CHALMERS
UNIVERSITY OF TECHNOLOGY

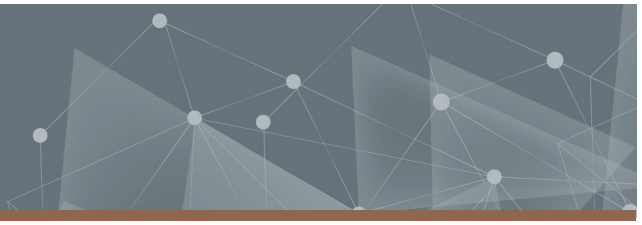

Blood Flow in Dissected Aortas After Thoracic Endovascular Aortic Repair

Master's thesis in Applied Mechanics

VISHAL SUBRAMANIASIVAM

DEPARTMENT OF MECHANICS AND MARITIME SCIENCES

CHALMERS UNIVERSITY OF TECHNOLOGY
Gothenburg, Sweden 2021
www.chalmers.se

Master's thesis 2021

Blood flow in dissected aortas after thoracic endovascular aortic repair

VISHAL SUBRAMANIASIVAM

CHALMERS
UNIVERSITY OF TECHNOLOGY

Department Of Mechanics And Maritime Sciences
Division of Fluid Dynamics
Chalmers University of Technology
Gothenburg, Sweden 2021

Blood flow in dissected aortas after thoracic endovascular aortic repair
Vishal Subramaniasivam

Thesis number: 2021:67

Supervisor: Håkan Nilsson, Department of Mechanics and Maritime Sciences
Johan Bondesson, Department of Mechanics and Maritime Sciences
Examiner: Håkan Nilsson, Department of Mechanics and Maritime Sciences

Master's Thesis 2021
Department of Mechanics and Maritime Sciences
Division of Fluid Dynamics
Chalmers University of Technology
SE-412 96 Gothenburg
Telephone +46 31 772 1000

Typeset in LaTeX
Gothenburg, Sweden 2021

Blood flow in dissected aortas after thoracic endovascular aortic repair
VISHAL SUBRAMANIASIVAM

Department of Mechanics and Maritime Sciences
Chalmers University of Technology

Abstract

Every passing hour, 2050 people die due to cardiovascular diseases, a third of them occurring prematurely before the age of 70. An aortic dissection is a condition where a sudden tear in the aortic wall forces blood to enter between the layers of the wall, subsequently splitting the wall and creating a new channel for blood. Untreated aortic dissections have a mortality rate of 80% at two weeks from the initial tear and treated aortic dissections have a mortality rate of 40% at five years. One treatment option is Thoracic Endovascular Aortic Repair (TEVAR), which involves placing one or several implants known as stent-grafts or endografts on the inner surface of the aorta. About 38% of TEVAR procedures come with post-procedural complications and approximately 19% to 24% require secondary re-interventions. Computational fluid dynamics (CFD) simulations can be used as a tool to predict post-procedural complications from a fluid mechanical perspective. In this study, the comparison of two post-surgical lumen scenarios is reported by conducting blood simulations using OpenFOAM, an open-source CFD tool. A study is also done on the non-Newtonian nature of blood and results are reported on the influence of using a non-Newtonian viscosity model as opposed to a Newtonian (constant viscosity) model. Validation of the computational grid and the viscosity model is done against experimental results retrieved from another study that used porcine blood.

Keywords: aorta, blood, non-Newtonian, viscosity, wall shear stress, TEVAR, OpenFOAM, vorticity, dissections, shear-thinning.

Acknowledgements

Professor Håkan Nilsson, thank you for giving me the opportunity to work on this thesis. Your expertise in the field of fluid mechanics and the resources that you provided were instrumental in conducting this thesis. I specially enjoyed it when I came to meetings filled with raw incoherent information I retrieved from literature over the week only for you to streamline it back to me in a sensible and logical way. Thank you for letting me explore, take my own decisions and most importantly for keeping the excitement of learning high.

Dr. Johan Bondesson, thank you for creating this project. Your support to strengthen the link between medicine and mechanics in this thesis has been instrumental. Listening to you explain the workings of the human aorta from both a medical and structural perspective has been enriching. Your eye for detail and your knack for filtering information has significantly helped this thesis and is something that I admire.

This computationally expensive thesis would not have been possible without the computational resources provided by Chalmers Centre for Computational science and Engineering (C3SE).

I am grateful for my family's unconditional love and support.

Vishal Subramaniasivam, Gothenburg, August 2021

Contents

1 Introduction **1**
- 1.1 Problem formulation . . . 1
- 1.2 Aim of the thesis . . . 3
- 1.3 Limitations . . . 3

2 Theory **5**
- 2.1 The cardiovascular system . . . 5
- 2.2 Properties of blood . . . 8
  - 2.2.1 Composition . . . 8
  - 2.2.2 Viscosity . . . 9
- 2.3 The thoracic aorta . . . 10
  - 2.3.1 Thoracic aortic anatomy . . . 10
  - 2.3.2 Thoracic aortic pathologies and the role of wall shear stress and vortices in their pathophysiology . . . 11

3 Methods **15**
- 3.1 Definition of study . . . 15
  - 3.1.1 Study A . . . 15
  - 3.1.2 Study B . . . 15
- 3.2 Geometry . . . 15
- 3.3 Computational fluid dynamics . . . 16
  - 3.3.1 Geometry . . . 17
  - 3.3.2 Computational mesh . . . 17
  - 3.3.3 Boundary conditions . . . 18
    - 3.3.3.1 Velocity . . . 18
    - 3.3.3.2 Pressure . . . 19
  - 3.3.4 Properties of blood . . . 19
  - 3.3.5 Solver settings . . . 20
- 3.4 Validation of grid and rheology . . . 20
- 3.5 Sectional views and data collection lines . . . 25

4 Results and discussions **27**
- 4.1 General flow features . . . 27
  - 4.1.1 Boundary layer development and vortex formation . . . 27
  - 4.1.2 Transformation of vortices into wall shear stress . . . 27
- 4.2 Newtonian model vs non-Newtonian model . . . 29

4.3 Luminal aorta vs abluminal aorta 35
4.4 Discussions 39

5 Conclusion **43**
5.1 Future work 43

1
Introduction

1.1 Problem formulation

The human cardiovascular system is made up of the heart, blood vessels and blood. Every passing hour, 2050 people die due to cardiovascular diseases, a third of them occur prematurely before the age of 70 [1]. From a fluid mechanical perspective the most common aortic diseases are aortic dissections, aortic aneurysms and atherosclerosis. This thesis focuses mainly on thoracic aortic dissections. An aortic dissection is a condition where a sudden tear in the aortic wall forces blood to enter between the layers of the wall, subsequently splitting the wall and creating a new channel for blood [40]. The pathology and pathophysiology of the disease will be elaborated more in the theory section of this thesis.

Untreated aortic dissections have a mortality rate of 80% at two weeks from the initial tear, and treated aortic dissections have a mortality rate of 40% at five years [21]. One treatment option is Thoracic Endovascular Aortic Repair (TEVAR), which involves placing one or several implants known as stent grafts or endografts on the inner surface of the aorta [9]. The stent graft is a thin metal mesh (the stent), covered with a thin polyester fabric (the graft). These implants not only serve to stop blood flow into tears in the aortic wall but also give structural integrity to the weakened blood vessel [4]. Figure 1.1 depicts a pre-TEVAR dissected aorta and a post-TEVAR dissected aorta.

The decision on the size and the placement of endografts as well as the precision and accuracy of the surgical intervention determines the outcome of such procedures. With several variables on the table, about 38% of TEVAR procedures come with post-procedural complications and approximately 19% to 24% require secondary re-interventions [18]. Some device-related complications include **endoleaks**, where there is a leakage of blood through or around endografts due to improper attachment, abnormal increase in porosity or damage from the forces of blood. **Endograft migration** is a condition where the implant moves more than 5-10mm from its intended placement due to hemodynamic forces. **Endograft collapse** involves the in-folding or collapse of the endograft, its development is attributed to large proximal aortic curvatures or blood pressure induced over-sizing of the endograft relative to the native aorta. **Malapposition** is a condition where a part of the stent-graft is not in direct contact with the vessel walls [18]. If the location of the malapposition is at the proximal end of the graft, this may lead to endoleaks between the walls of the implant and the natural wall of the aorta.

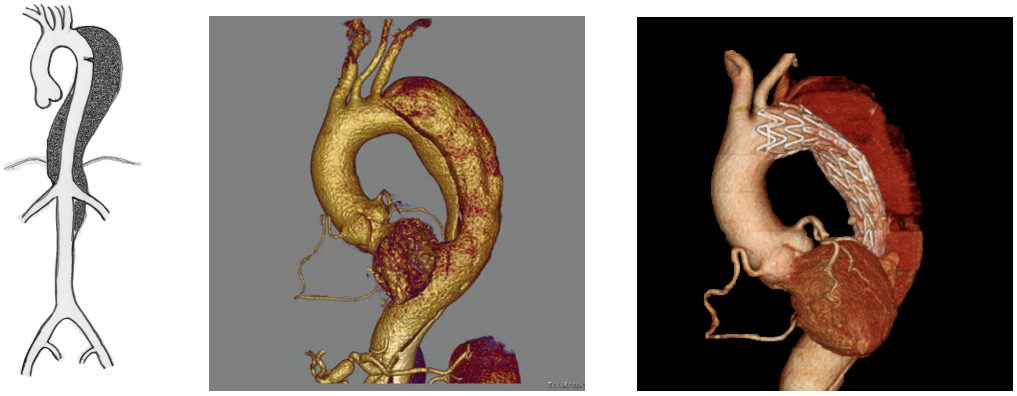

(a) **(b)** **(c)**

Figure 1.1: (a) Type B dissected aorta (clear vessel - true lumen, shaded vessel - false lumen), (b) CTA rendered image of Type B dissected aorta [10], (c) Type B dissected aorta post-TEVAR [10].

Advances in science and technology has given researchers imaging techniques that provide more information about the human aorta than ever and has also given the computational power that makes simulations faster than ever. Combining the two with Computational Fluid Dynamics (CFD) enables researchers to accurately conduct simulations of blood flow on digitally reconstructed aortas that have undergone TEVAR. Simulations can help forecast device related TEVAR complications as well as systemic ones that then can be treated before they occur [26].

Several research groups have run CFD simulations in aortas that have TEVAR implants [37, 36, 34, 6, 39, 48]. Though most of them provide numerical models for replicating clinical data, some groups focus mainly on the study of post-TEVAR complications such as malapposition [48, 6]. A common physical property that is studied not only by research groups dealing with fluid flow in post-TEVAR aortas but also by several groups researching on pathophysiology of common aortic conditions is wall shear stress. Dissections are believed to occur at regions of high wall shear stress [49, 3, 46, 36, 28]. Aneurysms and atherosclerosis are believed to occur at regions of low wall shear stress and oscillating wall shear stress [7, 24, 33, 45, 20, 38, 43]. Similarly, the movement of the stent graft and endoleaks is attributed to high torsional forces, that is shear stress incident at local points of the implant [35].

The biggest inconsistency between different research groups is the treatment of blood with respect to its rheology. Blood is a heterogeneous mixture of particles (erythrocytes, leukocytes, platelets, etc.) suspended in liquid plasma. The concentration of these particles, their interaction with each other and their interaction with surrounding structures are very complex and gives blood non-Newtonian properties (non-linear relationship between shear rate and shear stress) like shear-thinning, visco-elasticity, thixotropy and yield stress [44]. The latter two are only seen in the capillary levels of arteries. Shear-thinning (reduction of viscosity with increase in shear rate) happens in a small window of shear rates, any shear rate outside this

window will make blood a Newtonian fluid [7]. A majority of studies assume blood to be a Newtonian fluid on the premise that the shear rate in the entire aorta is much more than the window of shear rates that makes blood Newtonian. While this is true for healthy aortas, studies show non-Newtonian properties in complex aortic domains such as in dissections, aneurysms, aortas with TEVAR implants and atherosclerotic regions [31, 32, 25]. Several models are used to replicate the shear-thinning nature of blood [16]. The most successful of them in terms of validation with experiments is the Carreau-Yasuda model [8].

1.2 Aim of the thesis

With an overall objective to understand the flow of blood and its impact on post-TEVAR aortas, the aim of this project is further divided into the following three tasks:

- To understand the rheology of blood by validating the treatment of blood as a Newtonian and a non-Newtonian fluid against experimental results.
- Studying the relationship between vortical structures and wall shear stress while linking it to the geometry of the aorta and the viscosity of blood.
- Studying and comparing the Newtonian and the non-Newtonian rheological models on dissected aortas that have undergone TEVAR.
- Studying and comparing two post-surgical aortic geometries from a fluid mechanical perspective.

1.3 Limitations

The scope of this thesis is limited to the following list:

- The main region of interest in this thesis is the human thoracic aorta. Therefore, regions upstream like the heart and downstream like the abdominal aorta are excluded in the geometry.
- The geometries used are considered stationary with no fluid structure interaction.
- Boundary conditions prescribed are general in nature as opposed to accurate patient specific velocities and pressures.

2
Theory

2.1 The cardiovascular system

The human cardiovascular system is made up of the heart, blood vessels and blood. The role of the cardiovascular system in the human body can be broken into five main tasks, 1. transportation of oxygen and nutrients (e.g. glucose, amino acids) to all body tissues. 2. transportation of carbon dioxide and metabolic waste from body tissues to the lungs and the excretory system. 3. transportation of water, electrolytes and hormones throughout the body. 4. transport mechanism for the immune system 5. Regulation of the body temperature [2].

The entity that acts like a carrier to perform the above mentioned tasks is blood. Blood is a multi-phase suspension that consists of liquid plasma and suspended cells. The liquid plasma makes up 55% of blood and contains electrolytes, proteins and other molecules. The suspended cells make up the remaining 45 % of the blood and comprise erythrocytes, white blood cells and platelets [2]. A broader expansion into the composition of blood and its behaviour is discussed in the subsequent sections.

Blood is driven throughout the cardiovascular system by the heart, a muscular organ that is located just behind and slightly left of the breast bone. The heart acts as an elastic pump that under contraction creates a pressure head that drives blood throughout the body. The heart is divided into two sides, the left side and right side with two chambers each, an atrium and a ventricle per side. The chambers are separated by unidirectional valves that open when blood is transported from one chamber to the next. The tricuspid valve is located between the right atrium and the right ventricle. The pulmonary valve is located between the right ventricle and the pulmonary artery. The mitral valve is located between the left atrium and the left ventricle and finally the aortic valve is located between the left ventricle and the aorta [2].

A good starting point to explain the workings of the heart would be at the right atrium where deoxygenated blood from different parts of the body enters the heart, the blood from the right atrium is transferred to the right ventricle through a tricuspid valve. Contraction of the right ventricle pumps blood through the pulmonary valve to the lungs where the blood is oxygenated. The oxygen-rich blood is then transported back to the heart at the left atrium, the blood from the left atrium is transferred to the left ventricle through the mitral valve. Contraction of the left ventricle pumps blood through the aortic valve to the aorta where the blood is

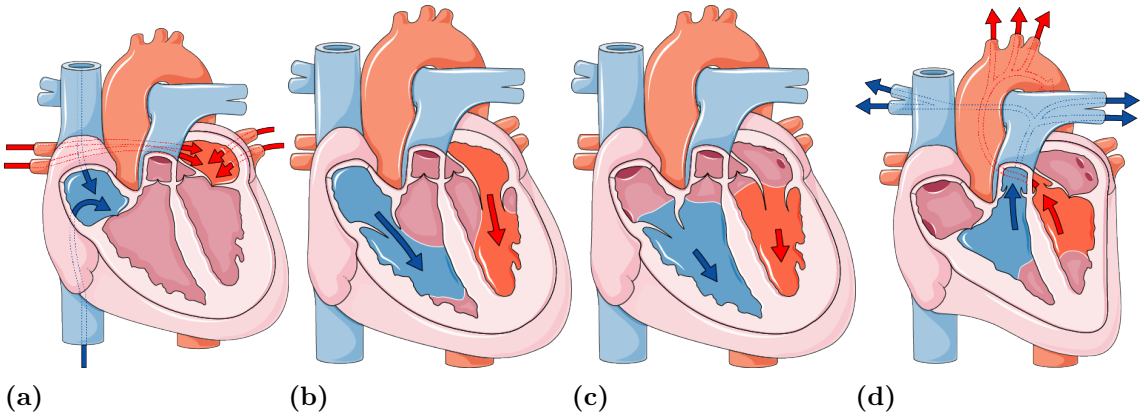

Figure 2.1: The flow of blood in the different chambers of the heart, (a) Blood entering the heart at the atriums, (b,c) Blood priming the ventricles, (d) Ventricular contraction pumping out blood into the aorta and the pulmonary vein.*Servier Medical art/CC BY-SA 3.0* [42].

transported to the rest of the body [2]. The flow of blood in the different chambers of the heart in one cardiac cycle is depicted in Figure 2.1.

Figure 2.2 gives an overview of the different pressures and volumes of blood at different stages of a typical cardiac cycle. Blood flows from the atrium to the ventricle when the pressure in the atrium is higher but blood cannot flow from the ventricle to the atrium when the pressure in the ventricle is higher as the chordae tendineae that anchor the mitral valve prevents blood flow into the atrium, similar is the case between the ventricle and the aorta. The Wiggers diagram in Figure 2.2 can be explained with the following points, 1. ventricular filling: the pressure in the left atrium is higher than the ventricle forcing blood to go through the mitral valve to fill up the left ventricle. 2. atrial systole: contraction of the left atrium ensures higher pressure at the left atrium which translates to flow of blood to the left ventricle. 3. isovolumetric contraction: as ventricles start contracting the pressure in the left ventricle becomes higher than that of the atrium, forcing the mitral valve to close. The pressure in the ventricle is lesser than that in the aorta, therefore there is no movement of blood but only an increase in the pressure in the ventricle. 4. ventricular Ejection: The isovolumetric contraction ends with the pressure in the left ventricle exceeding the pressure in the aorta, forcing blood to gush into the aorta. While the blood is depleted from the ventricle, the pressure in the ventricles drops and when it falls below that of the aorta, the aortic valve is forced to close starting the isovolumetric phase. 5. isovolumetric contraction: the pressure in the ventricle is falling but is lower than that in the aorta and higher than that in the atrium resulting in no exchange in volume. The isovolumetric contraction ends with the ventricular pressure dropping below the atrial pressure forcing the mitral valve to open thus starting the cycle once again.

The time period of one heartbeat is called a cardiac cycle and it can be broken down into two phases: systole and diastole. The period of ventricular contraction is termed systole and the period of relaxation is called diastole. The first sound

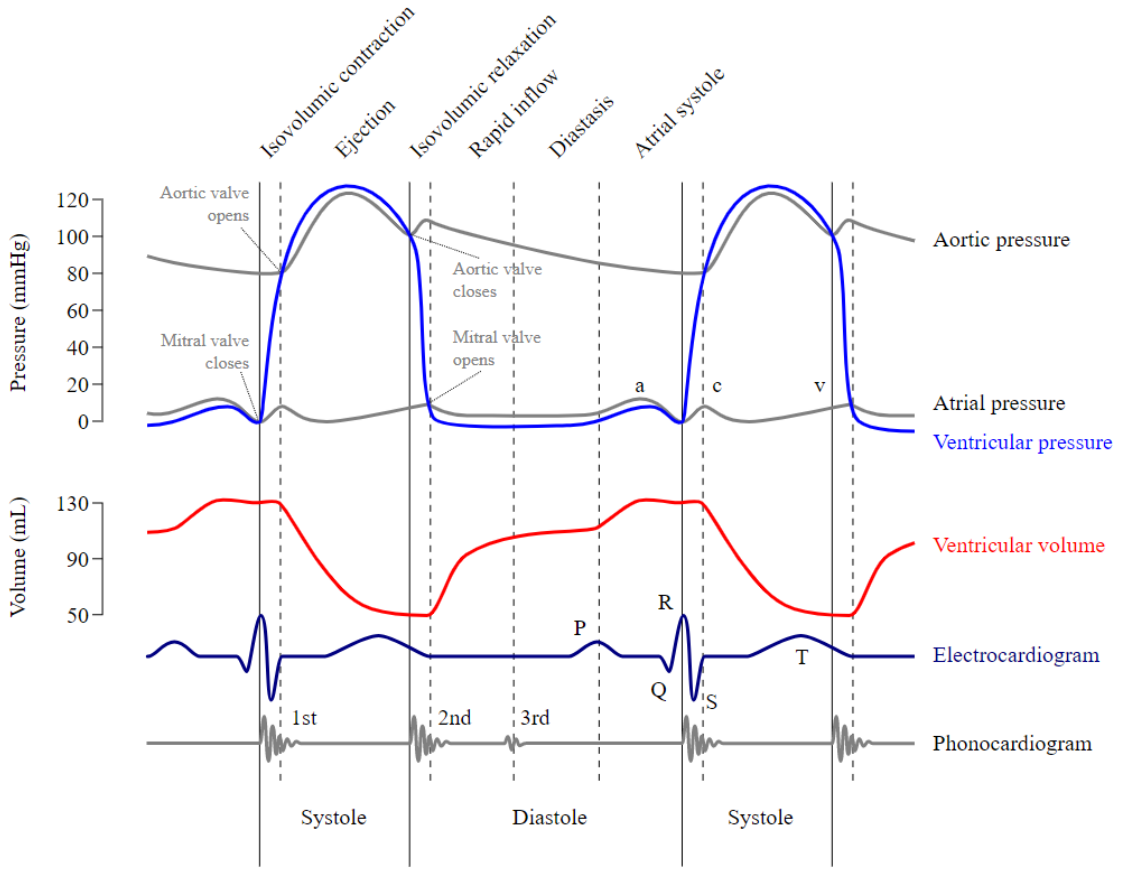

Figure 2.2: Pressure and volume at different chambers of the heart at different stages of a typical cardiac cycle *Daniel Chang MD, Wiki media Commons, CC BY-SA 2.5* [13].

of the heartbeat s1 (the lub) occurs when the mitral and the tricuspid valve close. The second sound of the heart beat s2 (the dub) occurs when the aortic and the pulmonary valves close.

The cardiovascular system can be classified with respect to the organs involved into two circuits, the pulmonary circuit and the systemic circuit. The pulmonary circuit is composed of arteries and veins that transport blood between the heart and the lungs. The pulmonary circuit starts at the right ventricle and ends at the left atrium, with its main role to carry the deoxygenated blood from the heart to the lungs for it to get oxygenated and then transports the oxygen-rich blood back to the heart. The systemic circuit on the other hand is composed of the arteries and veins that transport blood between the heart and every other organ in the body that requires blood. The circuit starts from the left ventricle pumping out oxygen-rich blood to every blood dependent part of the body and returns deoxygenated blood back to the heart to the right atrium [2].

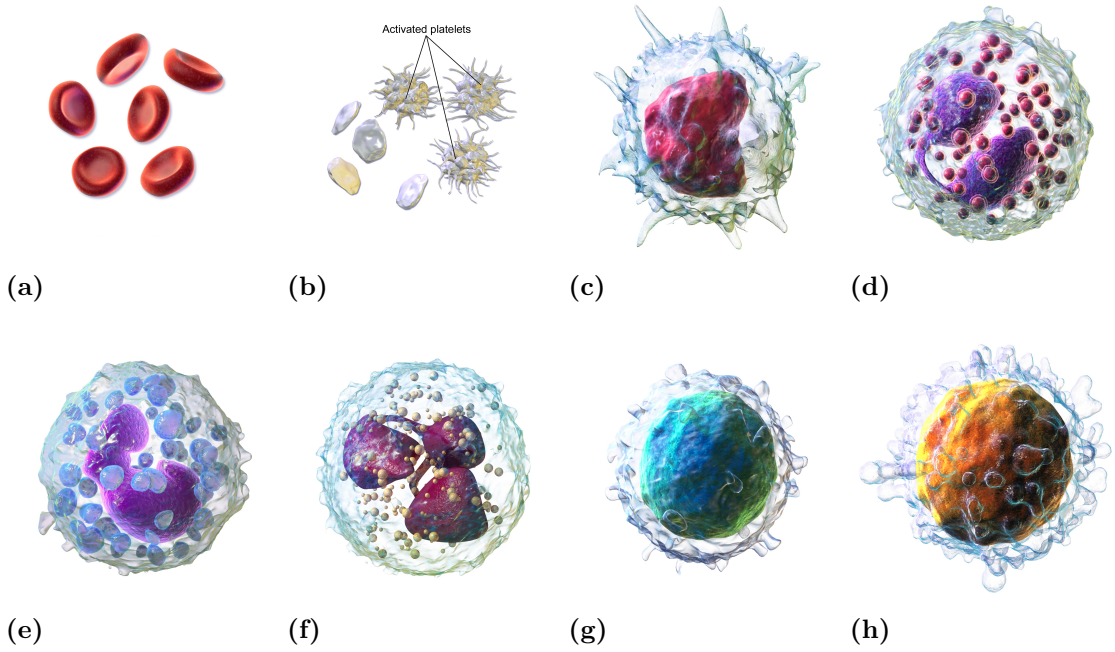

Figure 2.3: Different components that make up blood, (a) Erythrocytes, (b) Platelets, (c) Leukocytes-Monocyte, (d) Leukocytes-Eosinophil, (e) Leukocytes-Basophil, (f) Leukocytes-Neutrophil, (g) Leukocytes-Lymphocyte Bcell, (h) Leukocytes-Lymphocyte Tcell. *Bruce Blaus/Wiki media Commons/CC BY 3.0 and Servier Medical art/CC BY-SA 3.0* [42],[12].

2.2 Properties of blood

Blood acts like a transport system that transports several cells and chemicals that are required to perform tasks such as the delivery of oxygen and energy to tissues, removal of carbon dioxide and waste products from the tissues, transport of hormones, transport of signalling molecules and particles from the immune system to every nook and cranny of the body as well as regulation of temperature [2]. Therefore it is not just fluid but fluid with a plethora of particles suspended in it. Hence, it is important to study its composition and how its composition affects the way it flows.

2.2.1 Composition

As seen in Figure 2.3, blood can be broken down into three main groups, namely erythrocytes (41%), plasma (55%) and a mixture of leukocytes and platelets (4%). **Plasma** is the only fluid element in the blood. It has a density of 1025 kgm^{-3}, plasma is about 92% water, 7% proteins and the remaining 1% comprise of mineral salts, sugars, fats, hormones and vitamins [29]. **Erythrocytes** also known as red blood cells are by far the most number of cells in the blood. Red blood cells are biconcave discs with an effective diameter between 6.5 μm to 8.8 μm and contain a protein called haemoglobin that not only gives blood the distinct red colour but

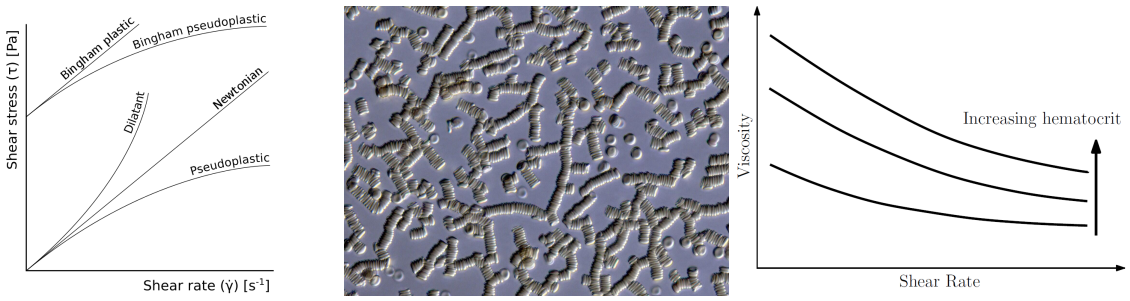

(a) **(b)** **(c)**

Figure 2.4: Different rheological behaviours of blood (a) Pseudo-plastic and Bingham pseudo-plastic behaviour of blood, (b) Rouleaux structures formed by erythrocytes, (c) viscosity as a function of hematocrit values. *g-sec/Wiki media Commons/CC BY 3.0 and Jonathan Armstrong/CC BY-NC 4.0* [14],[15].

also performs the task of carrying oxygen and carbon dioxide. **Leukocytes and platelets** are defensive cells in the bloodstream that defend the body against infection, foreign material and are part of damage control when different parts of the body are injured [29].

2.2.2 Viscosity

Blood is a heterogeneous mixture of particles mainly composed of erythrocytes, leukocytes and platelets along with other particles present in negligible concentrations, all of which are suspended in liquid plasma. The concentration of these particles are different in different individuals credited to different lifestyles, diets, health conditions, medications and other physical factors. The physical properties of these particles, their concentration in blood, their interaction with each other and their interaction with surrounding structures determines the rate at which blood strains when stress is applied on it, in other words it determines the viscosity of blood. The viscosity of a fluid gives the relationship between stress and strain when a force is acting on a fluid. Most fluids have viscosities that are constant irrespective of the forces applied on them and are called Newtonian fluids. Blood however portrays different viscosities depending on the forces applied on it and is called a Non-Newtonian fluid [44]. The different Non-Newtonian features portrayed by blood are:

1. **Shear thinning** - Erythrocytes at low shear rates aggregate, that is the formation of long 3D structures known as rouleaux due to the axial stacking up of erythrocytes as seen in Figure 2.4b. These long 3D structures act like obstructions to the flow, which translates to increase in local viscosity of the fluid. When the shear rate is increased in the flow (flow in bigger blood vessels) the high shear forces break the rouleaux structures, leading to a reduce in the viscosity of the blood. This reduction of viscosity at higher shear rates is called shear thinning or pseudo-plastic behaviour of blood which is essentially a non linear relationship between shear stress and shear rate as seen Figure 2.4a [44].

2. **Viscoelasicity** - Each erythrocyte is elastic in nature. The elastic effect is magnified with the aggregation of these the erythrocytes that forms the 3D rouleaux structures. The elasticity in these 3D structures is significant enough to cause change in local viscosity of the fluid. This effect is further increased with the increase in the number density of erythrocytes, as seen in Figure 2.4c [44].

3. **Yield stress** - At extremely high agglomeration that is typically found at small capillaries, blood as a fluid does not shear until a minimum threshold stress is available to act on it. After the minimum threshold is hit the blood behaves like a pseudoplastic liquid (shear thinning liquid) and is called a Bingham pseudo-plastic. The pseudoplastic and Bingham pseudoplastic behaviour of blood is compared against a Newtonian (linear) relation between shear stress and shear rate in Figure 2.4a [44].

2.3 The thoracic aorta

2.3.1 Thoracic aortic anatomy

The aorta is the largest and the first blood vessel in the systemic circuit, originating from the aortic valve at the left ventricle of the heart and extending down till the abdomen where it branches into smaller arteries. The thoracic aorta however is a section of the aorta that begins at the aortic valve and ends when the aorta passes through the diaphragm. The different parts and branches of the thoracic aorta are illustrated in Figure 2.5a. The thoracic aorta can be broken further into three subsections: the ascending aorta, the aortic arch and the descending aorta. The ascending aorta begins at the aortic root where the right and left coronary arteries that provide blood to the muscles of the heart are situated and ends just before the brachiocephalic artery. The aortic arch arches over the heart and changes the direction of blood by guiding blood towards the abdomen. Three arteries branch off and also mark the proximal and distal ends of the aortic arch: the brachiocephalic artery that takes blood to the right arm and parts of the head, the left common carotid artery that supplies the head with blood and the left subclavian artery that provides blood to the left arm and other parts of the upper body. Downstream of the aortic arch is the descending aorta that has its distal end at the diaphragm [2].

The wall of the aorta can be viewed as a three-layered structure, as illustrated in Figure 2.5b. The **tunica intima** is the innermost layer and is comprised of the endothelium (endothelial cell mono-layer) and connective tissues. The endothelial cells that are in contact with the lumen (space in the aorta where the blood flows) control vascular permeability, vasoconstriction, regulation of haemostasis and growth of new blood vessels. The **internal elastic lamina** is a perforated elastic layer that separates the **tunica intima** from the second layer, the **tunica media**. The tunica media contains smooth muscle cells structured in an extracellular matrix composed mainly of elastin, collagen and protoglycans. The main function of this layer is to provide the aorta with enough elasticity so as to withstand the magnitude of pulsating pressures in the blood. The **external elastic lamina** is a perforated elastic layer that separates the **tunica media** from the outermost layer, the **tunica adventitia**. The tunica adventitia is almost entirely filled with connecting fibres and

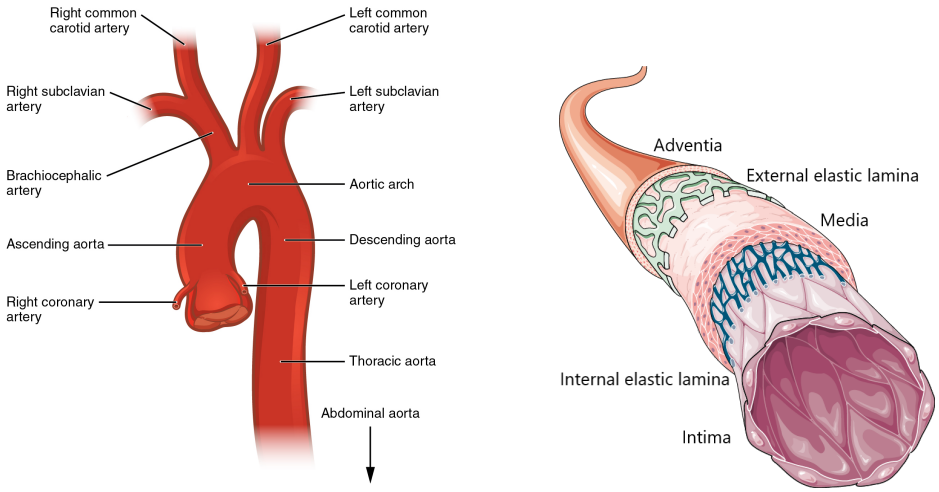

Figure 2.5: (a) The thoracic aortic anatomy including branch vessels, (b) Key structural features of the Aorta, *Openstack-collage/Wikimedia Commons/CC by 3.0 and ServierMedical art/CC BY-SA 3.0* [42].

an external lamina to anchor the vessel to surrounding tissues. Two proteins that are present in all the three aforementioned layers are **elastin** and **collagen**. Elastin are molecular springs that allow the aorta to expand during systoles and contract during diastoles. The collagen function as a framework that anchors smooth muscles in place during pulsating pressures when the aorta contract and expand [2].

2.3.2 Thoracic aortic pathologies and the role of wall shear stress and vortices in their pathophysiology

As presented in the introduction, this thesis will mainly work on thoracic aortic dissections. Nevertheless, this section will discuss other life-threatening conditions in the aorta to build a case on the influence of wall shear stress and vorticity in the pathophysiology of these conditions.

Aortic dissections

An aortic dissection is an event in the aorta when a sudden tear in the intima results in blood leaking between the layers of the aortic wall, forcing the layers of the wall to split. The split between the layers of the wall is further propagated by the pressure of the leaking blood. As a result, there is a separate channel that is created between the layers of the wall called the false lumen as opposed to the true lumen which is the natural path of the blood [40]. In many cases the pressure in the false lumen becomes significantly high enough at a local point to force the creation of a re-entry tear, where the blood re-enters from the false lumen to the true lumen. A consequence of the formation of the false lumen is the reduction in diameter of the true lumen [40].

Over time the blood in the false lumen may clot, resulting inflow of blood only in the true lumen with a reduced diameter. If the false lumen provided blood to any other

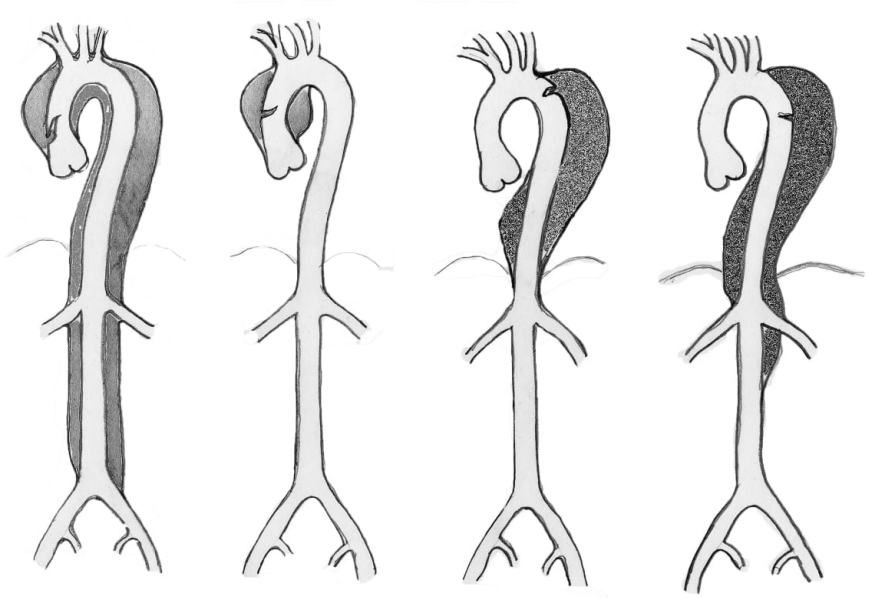

Figure 2.6: The Stanford classification of aortic dissections, starting from the left, first two Stanford A and the following Stanford Type B.

organ, clotting of the false lumen can cause blood to be cut off from the organ. In certain cases, the outer layer of the false lumen ruptures leading to blood flowing out of the aorta and subsequently dropping the blood pressure [22]. Aortic dissections can be classified based on the location of inception of the intimal tear. Stanford type A dissections involve the intimal tear at the ascending aorta and Stanford type B dissections involve the intimal tear distal to the subclavian artery, as illustrated in Figure 2.6.

Tears that occur at the ascending aorta are attributed to high hemodynamic and torsional forces in the blood that increase the wall shear stress at the wall [27]. The high torsional forces at the ascending aorta is because of the close proximity to the high-velocity output flow from the aortic valve as well as the fact that the aorta forces the blood to turn a heavily obtuse angle from the ascending aorta. Most tears at the descending aorta usually occur in patients suffering from hypertension and the site of the tear is at a specific region situated just distal to the subclavian artery. This specific point separates the mobile aortic arch which heavily displaces due to hypertension and the fixed descending aorta that is bounded to the spine, therefore experiencing high shear forces [19]. Another major factor that causes dissection is the wall losing its elasticity mainly due to the loss of elastin and collagen, which can occur due to different genetic connective tissue disorders like Marfan's and Ehlers-Danlos syndromes or due to a previous episode of atherothrombosis or aneurysms at the very location. More on atherothrombosis and aneurysms are discussed in the following paragraphs [41].

Aortic aneurysms

Aortic aneurysms occur when the aortic wall is locally weakened causing dilation of

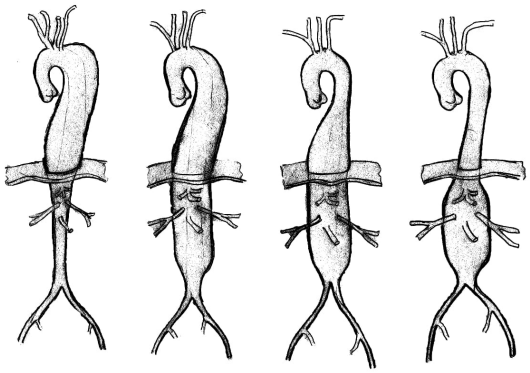

Figure 2.7: Illustration of different locations of Aortic aneurysms.

the aorta. This dilation can either rupture, be the initial stage of aortic dissection or the blood in it can clot-forming an intraluminal thrombus [30]. Aneurysms can be classified based on the location of the dilation, as shown in Figure 2.7. The cause of aneurysms is believed to be due to the irreversible degradation of elastin and collagen in the arterial wall, which can be due to many underlying factors such as genetic connective tissue disorders, hypertension and atherosclerosis [17].

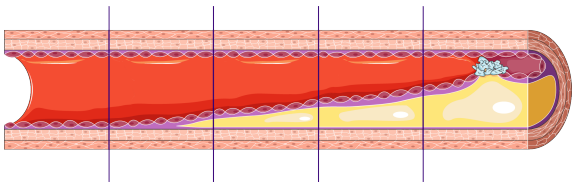

Figure 2.8: Pathophysiology of atherosclerosis over time starting from the left at the time of inception to the right *ServierMedical art/CC BY-SA 3.0*[42].

Atherosclerosis

Atherosclerosis is the most common vascular disease that involves the accumulation of low-density lipoprotein in the arterial wall. The particles that enter the wall accumulate and eventually clot with other debris [23]. This not only reduces the luminal cross-section but may also rupture leading to clotted debris also known as atherosclerotic plaque clogging up different arteries leading to a halt in blood flow. Atherosclerosis in the wall of the aorta causes the depletion of elastin and collagen in the wall, the rupture of small atherosclerotic plaques may not cause blocks or heart attacks but can expose regions with low elasticity to contact with blood, this can further lead to aortic aneurysms and aortic dissections [7].

3
Methods

3.1 Definition of study

As presented in the introduction (Section 1.2), the aim of this thesis can be broken into two studies, one studying the rheology of blood flow in an aorta and the other comparing blood flow between two post-TEVAR lumen scenarios. The details of the two studies are discussed in the following two subsections.

3.1.1 Study A

Blood depending on its location in the body as discussed in section 2.2.2 portrays non-Newtonian characteristics like shear-thinning, visco-elasticity and yield stress. The difference in flow characteristics between a Newtonian model and a non-Newtonian model for blood is analysed by simulating the respective flows in a dissected aorta that has undergone thoracic endovascular aortic repair, the geometry of which is generated from computed tomography angiography (CTA).

3.1.2 Study B

The geometry of a blood vessel determines the magnitude and orientation of vortical structures, this also means it subsequently determines the magnitude and orientation of local wall shear stress on the vessel walls. Study B compares the flow of blood between two post-TEVAR lumen scenarios, an actual post-TEVAR lumen generated from CTA vs a hypothetical post-TEVAR lumen.

3.2 Geometry

In this study, two different models of the aorta are used. The first model (luminal aorta) was provided by another research group [10], who research on modelling techniques in the cardiovascular system. The provided model was generated using images from CTA, where x-ray images are captured while a contrast fluid is injected into the blood flow to enhance the path of blood in the vessel. The images from the CTA were processed into stereo-lithographic format files (STL) using SimVascular [47], an open source tool developed for manual and semi-manual modeling of the vascular system.

As seen in Figure 3.1a and Figure 3.1b, the first model has two endografts present,

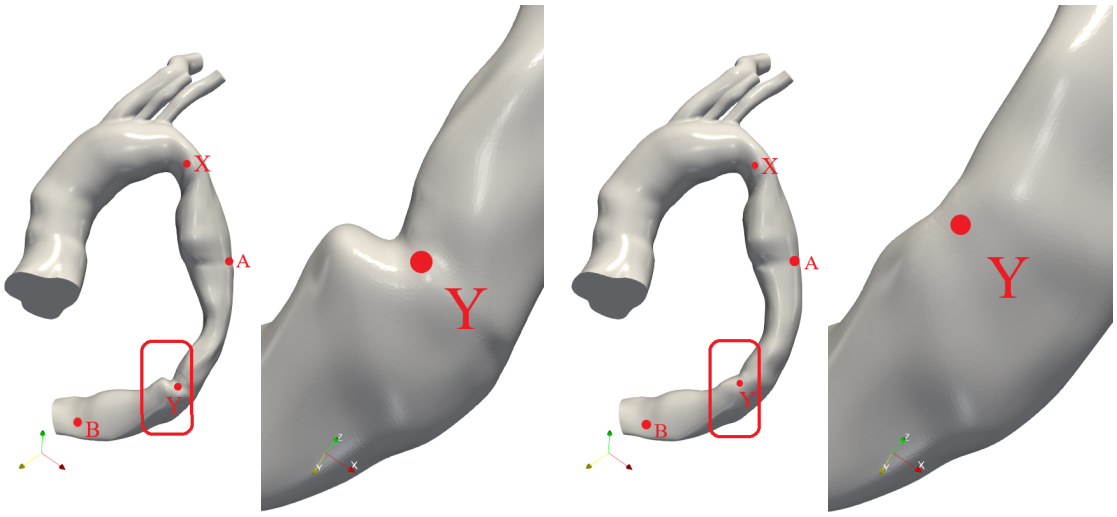

(a) **(b)** **(c)** **(d)**

Figure 3.1: (a) Luminal aorta with point X and point Y representing proximal and distal end of the endograft 1, point A and point B representing proximal and distal end of the endograft 2, (b) Point Y zoomed in, (c) Abluminal aorta with point X and point Y representing proximal and distal end of the endograft 1, point A and point B representing proximal and distal end of the endograft 2, (d) Point Y zoomed in.

X-Y representing endograft 1 and A-B representing endograft two. An important feature to be noted from the first model is the sudden increase in the area of the lumen when the the flow encounters the transition between endograft 1 and endograft 2. This abrupt jump is due to the malapposition of the two endografts (endograft 1 is not placed in flush with endograft 2 at the distal end of endograft 1).

The second model (abluminal aorta) was modelled with the aim to eliminate malapposition of the two endografts. This is done as a hypothetical scenario where the endograft 1 is placed in flush with endograft 2 at the distal end of endograft 1, as seen in Figures 3.1c and 3.1d. The modelling of the abluminal aorta is also done using SimVascular [47].

3.3 Computational fluid dynamics

All the blood flow simulations in this thesis was performed using OpenFOAM, an open source numerical solver written in C++ and used for computational fluid dynamics. The versions used in this thesis were OpenFOAM v2006. The following subsections will give a deeper insight into the different parameters and settings defined while carrying out the simulations.

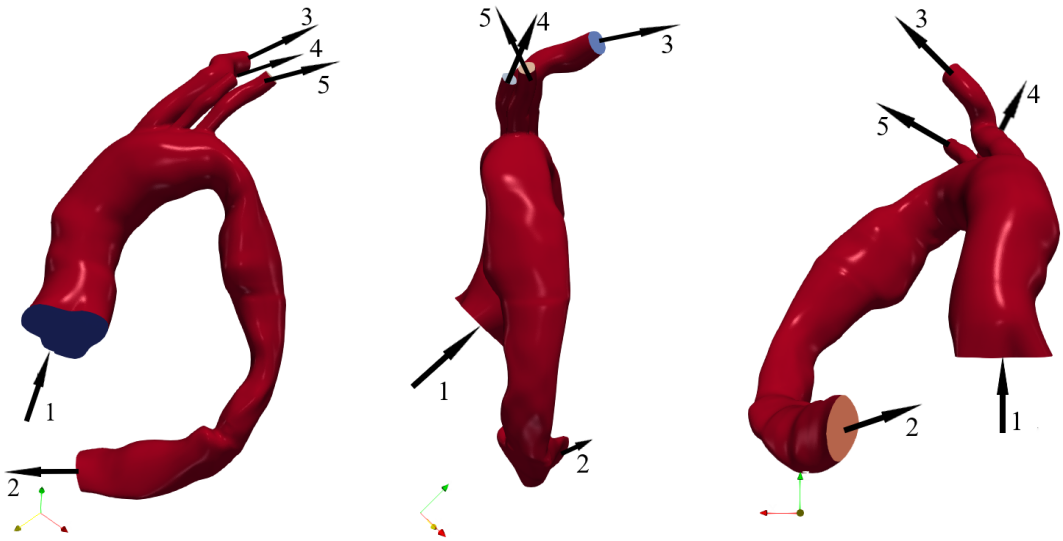

(a) **(b)** **(c)**

Figure 3.2: Different views of the luminal geometry used, illustrated with (1) inlet from the heart , (2) Main outlet to the abdominal aorta , (3) outlet to the brachiocephalic artery , (4) outlet to the left common carotid artery and (5) outlet to the left subclavian artery . (a) Front view,(b) Side view,(c) View with the inlet plane parallel to the x-y plane.

3.3.1 Geometry

The geometries that are modelled in SimVascular from raw CTA images as explained in Section 3.2 are further modified in Blender, an open source 3D modelling tool. Using Blender the geometry is prepared for OpenFOAM which involves making sure the model is water-tight and does not have any surface triangulation discrepancies. Blender is also used to define and rename different planes in the STL file as depicted in Figure 3.2, which allows OpenFOAM to understand where boundary conditions have to be applied.

3.3.2 Computational mesh

The STL flies that are prepared as a result of CTA imaging, modelling and surface fixing are now ready to be broken down into a computational mesh. The *snappyHexMesh* and *BlockMesh* utilities in OpenFOAM v2006 are used to break down the luminal and the abluminal models into smaller elements, that is further discretized to solve fluid governing equations on them. Table 3.1 gives information on the computational mesh used for both the geometries in this study. 10 prism layers are defined with an average total layer height of 0.000384m to capture the development of the boundary layer. The mesh for the luminal aorta has 18.70 million cells and the mesh for the abluminal aorta has 18.66 million cells. Though the abluminal aorta has a higher overall volume, the higher surface complexity of the luminal aorta

results in more mesh elements to capture the surface accurately.

Mesh parameters	Luminal aorta	Abluminal aorta
Grid size - Δx_{min}	0.00022 m	0.00023 m
Grid size - Δy_{min}	0.00020 m	0.00020 m
Grid size - Δz_{min}	0.00023 m	0.00025 m
Number of prism layers	10	10
Average total prism layer height	0.000384	0.000384
Percentage of surface with prism layers	99%	98.9%
Number of mesh elements	18.70 million	18.66 million

Table 3.1: Meshing parameters and statistics for the luminal and the abluminal geometries.

3.3.3 Boundary conditions

This section summarises the different boundary conditions defined prior to the simulation of flow, as tabulated in Table 3.2. A zero gradient pressure boundary condition is defined for all the boundaries except the main outlet. A volume flow rate boundary condition is defined for all inlets and outlets except the main outlet where a zero gradient velocity is applied. The velocity and pressure boundary conditions are further explained in the succeeding subsections.

Boundary	**Pressure**	**Velocity**
Inlet	Zero gradient	Volume flow rate
Main outlet	Fixed value	Zero gradient
Brachiocephalic outlet	Zero gradient	Volume flow rate
Left common carotid outlet	Zero gradient	Volume flow rate
Left subclavian outlet	Zero gradient	Volume flow rate
Wall	Zero gradient	no slip

Table 3.2: Velocity and pressure boundary conditions applied to different inlets and outlets.

3.3.3.1 Velocity

The rate of blood flow into the aorta from the heart is not the same for every individual, it varies from person to person depending on the individual's overall

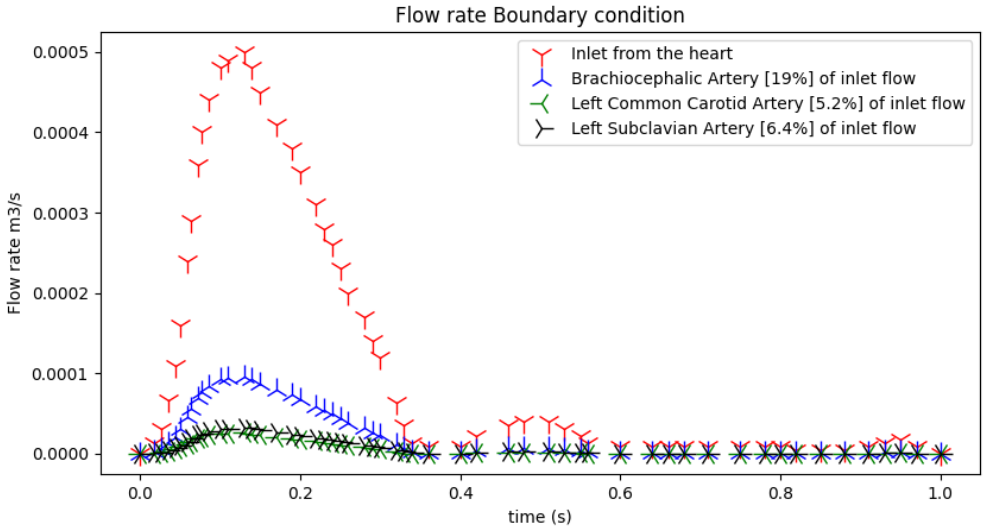

Figure 3.3: Volume flow rate vs time defined for the inlet, branchiocephalic artery, left common carotid artery and the left subclavian artery.

health [2]. Nevertheless, since this thesis is a comparative study, a general flow-rate boundary condition is obtained taking inspiration from another study [5]. As depicted in Figure 3.3, volume flow rate is defined for one full cardiac cycle at different locations of the aorta. The waveform for the inlet of the aorta is the same as the ventricular output from the heart, that is the flow of blood into the aorta only during the systolic part of the cardiac cycle after which the aortic valve is shut off so than blood can fill-up the left ventricle. The outlet flow rates at the different branches of the ascending aorta are defined as a percentage of the inlet flow rates. That is 19% of the inlet flow goes to the branchiocephalic artery, 5.2% to the left common carotid artery and 6.4% to the left subclavian artery. The remaining 69.4% of the blood goes as an output of the thoracic aorta.

3.3.3.2 Pressure

A zero gradient pressure boundary condition is defined at the inlet and at the branches rooting at the aortic arch. A zero pressure boundary condition is defined at the main outlet of the geometry. Therefore, all pressures depicted in this study are considered relative to the zero pressure at the main outlet.

3.3.4 Properties of blood

As discussed in Section 2.2.2, blood in many cases behaves as a non-Newtonian fluid displaying properties of shear-thinning, thixotropy and visco-elasticity. Although many studies assume that blood behaves like a Newtonian fluid in big blood vessels like the aorta, it is also considered as a non-Newtonian fluid in deceased aortas that have irregular or constricted geometries. To investigate the impact of the blood's rheology, two different models, one Newtonian and the other non-Newtonian is considered in the present work.

The Newtonian model is considered with a constant dynamic viscosity of $\mu = 0.0044Pas$ [7]. The Carreau-Yasuda model [8] was used to include the shear-thinning nature of blood. The Carreau-Yasuda model is defined as

$$\frac{\mu - \mu_\infty}{\mu_0 - \mu_\infty} = [1 + (\lambda\dot{\gamma})^a]^{\frac{(n-1)}{a}}.$$

$\dot{\gamma}$ denotes shear rate. $\mu_\infty = 0.16Pas$ and $\mu_0 = 0.0035Pas$ set the lower and upper end of the viscosity ranges respectively, and the constants $\lambda = 8.2$, $a = 0.64$ and $n = 0.2128$ define the transition of viscosity within the prescribed ranges as a function of shear rate.

The density of blood defined in the simulations is $1050kg/m^3$. The density is calculated as a weighted average of its general composition, 41% erythrocytes ($1090kg/m^3$), 4% Leukocytes ($1030kg/m^3$) and 55% plasma ($1025kg/m^3$).

3.3.5 Solver settings

In this study it is assumed that the duration of a cardiac cycle is 1 second. The simulation is run for a total of 2 seconds, that is two cardiac cycles. The results are retrieved only for the second cardiac cycle to account for residue vortices present after each cycle. The boundary conditions and physical properties of blood are discussed in previous sections. A time step of $10^{-5}s$ was used during the systolic phase of the cardiac cycle simulation to ensure a maximum Courant number of 0.7. Since the velocity of flow is negligible during the diastolic phase of the cardiac cycle, the time step was modified to $10^{-3}s$.

The PIMPLE (Pressure Implicit Method for Pressure-Linked Equations) algorithm is used for pressure-velocity coupling. The pressure equation is solved using GMAG solver and the equations for velocity use smoothSolver. The bounded Gauss linear-upwind scheme is used to discretize the convective terms of the governing equations. The implicit second-order backward scheme is used to discretize the time derivative terms and the second order least-squares method to calculate gradients.

3.4 Validation of grid and rheology

To ensure that the results implementing the Newtonian model, the non-Newtonian viscosity model and the mesh strategy is reliable and viable, the viscosity models (Newtonian and Carreau-Yasuda model) and the mesh from this thesis is verified against experimental data from another study [25].

Experimental setup (Performed by [25])

The geometry used in the experiment is that of the bifurcation in the human common carotid artery which was manufactured using plexiglas. The experiment involves the use of an optical laser probe and sensors that captures velocity signals in fluid flows. For the Newtonian fluid a concentrated solution of potassium thiocyanata is mixed in water to match the desired viscosity of blood. Potassium thiocyanata portrays

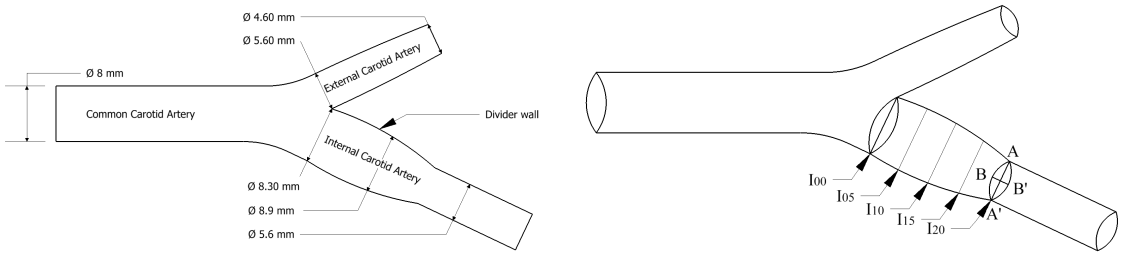

(a) **(b)**

Figure 3.4: (a) Geometry of the bifurcation in the common carotid artery manufactured and implemented in the experiment, (b) Definition of measurement sites along two orthogonal planes ([A-A'] and [B-B']).

a transparency and refractive index that is suitable for the optical measurement devices used. To bring in the effect of the non-Newtonian fluid, 250 ppm xanthan gum is mixed to the previous solution. The non-Newtonian fluid portrays a very similar rheology to that of porcine blood, which is known to mimic the rheology of arteries and arterioles. A validation study done by [11] to compare the rheology of the synthesized fluid (aqueous solutions of xanthan gum) with porcine blood reports agreeable similarity in capturing the shear-thinning and visco-elastic nature of blood.

The geometrical features as well as the data retrieval planes are illustrated in Figure 3.4. The geometry is basically the bifurcation of the common carotid artery into the external carotid artery and the internal carotid artery. The experimental retrieval of data is done in the proximal portion of the internal carotid artery at five measurement sits at different axial positions namely I01, I05, I10, I15 and I20 at two orthogonal planes ([A-A'] and [B-B']).

CFD setup (Performed as part of this thesis)

A steady state simulation of blood flow in the common carotid artery bifurcation was performed in OpenFOAM v2012. A Reynolds number of 270 was defined at the common carotid artery with 68.9% of the flow going to the internal carotid artery outlet and 31.1% of the flow going to the external common carotid artery. A fully developed velocity profile is given at the entrance of the common carotid artery. The rheology of blood assumed in this validation study is the same as that defined in 3.3.4. With the exception that this validation study is a steady state simulation, the remaining solver settings are same as that defined in 3.3.5. Table 3.1 gives information on the computational mesh used. The computational mesh has a total of 716,000 elements.

CFD validation results

Figures 3.5 and 3.6 compare the Newtonian experimental results with the Newtonian model from the current study. Figures 3.7 and 3.8 compare the non-Newtonian

Mesh parameters	Luminal aorta	Common carotid artery
Grid size - Δx_{min}	0.00022 m	0.00019 m
Grid size - Δy_{min}	0.00020 m	0.00020 m
Grid size - Δz_{min}	0.00023 m	0.00019 m
Number of prism layers	10	10
Average total prism layer height	0.000384	0.000310
Percentage of surface with prism layers	99%	97%
Number of mesh elements	18.70 million	716 thousand

Table 3.3: Meshing parameters and statistics for the common carotid artery and the luminal aorta.

experimental results with the Carreau-Yasuda model from the current study. It can be noted that the velocity contours from the current study satisfyingly match the velocity contours from experimental results. As seen in Table 3.3, a similar mesh size and meshing strategy was used both for the validation study and for the primary study (luminal and abluminal). This, added with the fact that the same viscosity models were used, validates the mesh and the viscosity models used for the primary study in this thesis. Therefore, the results in the luminal and the abluminal cases pertaining to quantities such as velocity, viscosity and their derivatives (vorticity, wall shear stress) can be trusted to behave very similarly to real life blood flow.

Fully developed flow from the common carotid artery inlet is incident at the apex that bifurcates between the external carotid artery and the internal carotid artery. Since it is a fully developed flow, the highest velocity before the bifurcation is at the center of the geometry (at the apex). Therefore, as seen in the A-A' plane (Figure 3.5 and Figure 3.7), higher velocities are seen towards the divider wall. The cross-sectional area increases from I_{00} to I_{10} and reduces from I_{10} to I_{20}, therefore the flow expands and contracts leading to an increase in velocity gradients. The velocity gradients are steeper in the Newtonian case when compared to the non-Newtonian case, the reason being that the Carreau-Yasuda model reduces the viscosity at high velocity gradients making the flow less obstructive. At the same time the Carreau-Yasuda model increases the viscosity at low shear rates making the flow more obstructive. Therefore, the velocity profiles for the Carreau-Yasuda model are relatively smoother than than that of the Newtonian constant viscosity model.

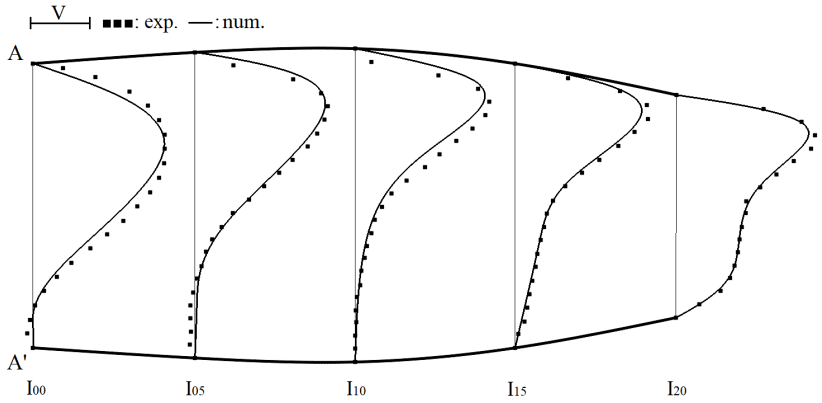

Figure 3.5: Experimental velocity profiles compared with numerical velocity profiles for the Newtonian scenario at plane A-A'.

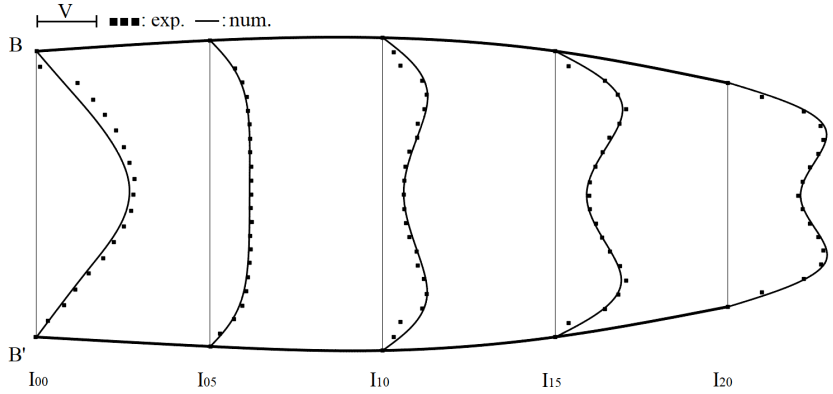

Figure 3.6: Experimental velocity profiles compared with numerical velocity profiles for the Newtonian scenario at plane B-B'.

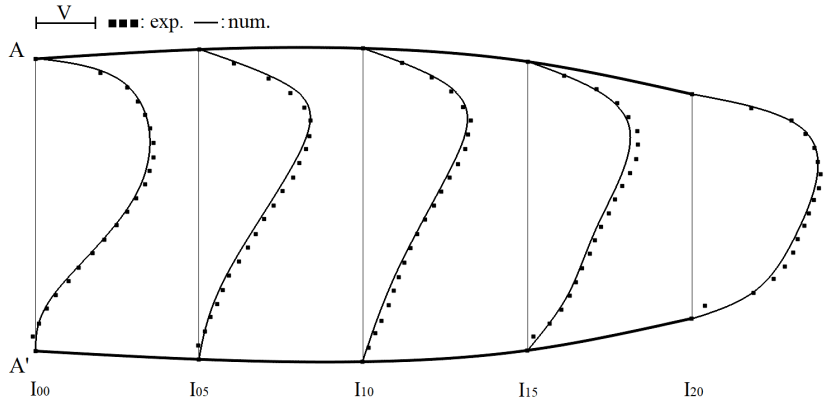

Figure 3.7: Experimental velocity profiles compared with numerical velocity profiles for the non-Newtonian scenario at plane A-A'.

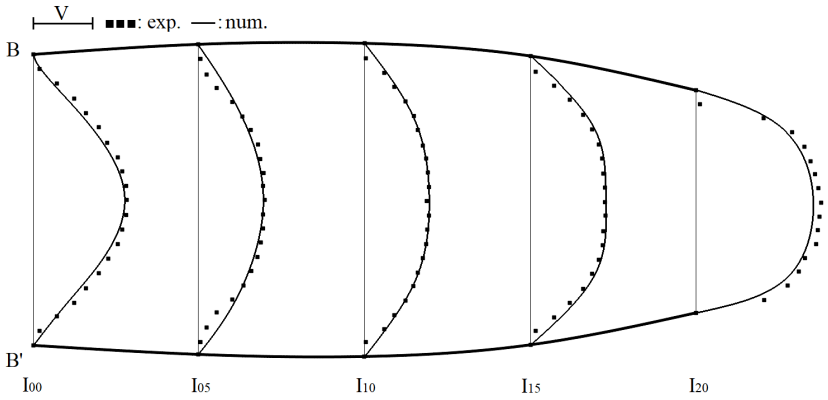

Figure 3.8: Experimental velocity profiles compared with numerical velocity profiles for the non-Newtonian scenario at plane B-B'.

3.5 Sectional views and data collection lines

This sub-section is dedicated to defining the different planes and lines that are used to collect, plot and visualize data. Figure 3.9 depicts the definition of sectional-view-1, where a planar slice is created along the axial center of the thoracic aorta. Figure 3.10 depicts the definition of sectional-view-2, where a planar slice is created along the axis of the descending thoracic aorta, the intersection of the planar slice with the wall defines the inner and outer data collection lines. The inner line being on the inner curve of the aorta and the outer line being on the outer curve of the aorta. Figure 3.11 depicts the definition of sectional-view-3, where a spherical slice is created along the axis of the descending thoracic aorta, the intersection of the spherical slice with the wall defines the anterior and posterior data collection lines. The anterior line faces the chest of the patient and the posterior line faces the back of the patient.

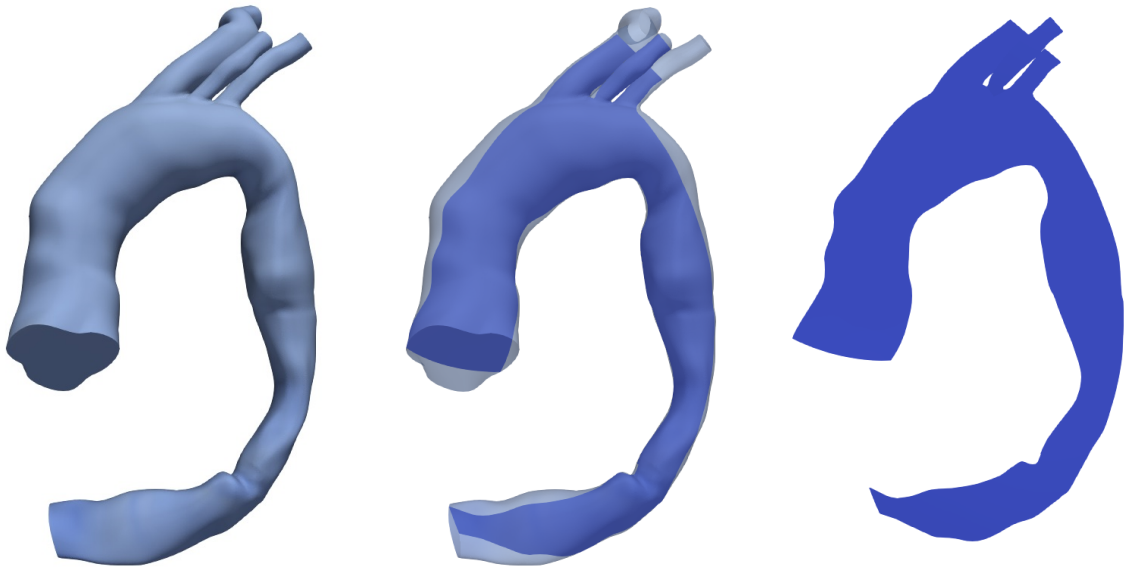

(a) **(b)** **(c)**

Figure 3.9: Definition of **sectional-view-1**,(a) 3D structure of the aorta as described in section 3.1,(b) 2D plane depicted in the transparent 3D structure,(c) **Sectional-view-1**.

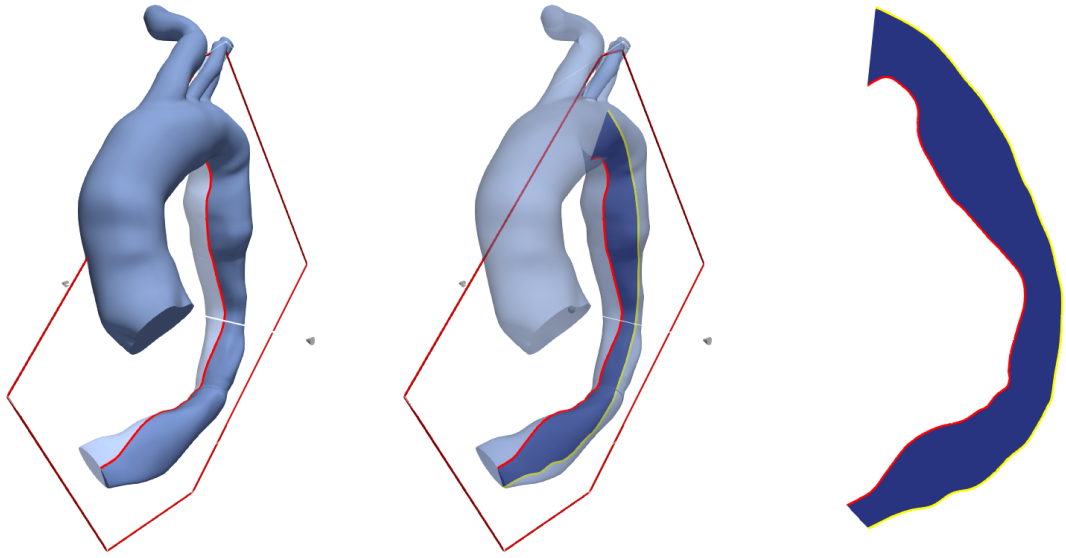

(a) **(b)** **(c)**

Figure 3.10: Definition of **sectional-view-2**, **inner line** and **outer line**, (a) 3D structure of the aorta as described in section 3.1,(b) 2D plane depicted in the transparent 3D structure,(c) **sectional-view-2**, (—, **red**) inner data collection curve, (—, **yellow**) outer data collection curve.

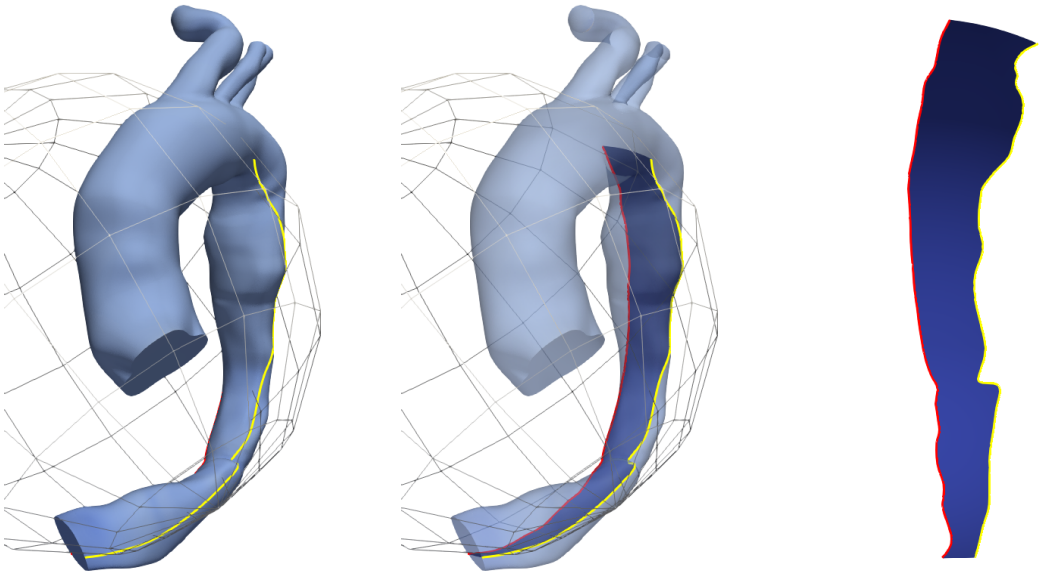

(a) **(b)** **(c)**

Figure 3.11: Definition of **sectional-view-3**, **anterior line** and **posterior line**, (a) 3D structure of the aorta as described in section 3.1,(b) spherical plane depicted in the transparent 3D structure,(c) **sectional-view-3**,(—, **yellow**) anterior data collection curve,(—, **red**) posterior data collection curve.

4

Results and discussions

Results and discussions presented in the following subsections are retrieved from four simulations. With an objective to compare the effects of Newtonian and non-Newtonian viscous models, two simulations are run respectively on the luminal aorta. With an objective to compare the effects of the luminal and the abluminal aortic models, two simulations are run respectively with the non-Newtonian viscosity model. The different views depicted in the contours are defined in section 3.5.

4.1 General flow features

4.1.1 Boundary layer development and vortex formation

The simulations on the thoracic aortas have been done with a time changing velocity boundary condition as discussed in Section 3.3.3. The boundary layer development and vortex formation during systolic blood flow is of importance when compared to diastolic blood flow as there is no significant flow of blood during the diastolic part of a cardiac cycle. Figure 4.1 depicts the contours of vorticity for the first 0.3 seconds of the cardiac cycle. As previously discussed in the explanation about Figure 3.3, fluid that enters the aorta accelerates for the first 0.13 seconds then decelerates till 0.38 seconds, after which inlet flow is negligible.

The no-slip boundary condition that is prescribed on the walls of the aorta create high velocity gradients at the walls, creating high rotational flow in the form of vortices near the walls. The building up of boundary layers in the transverse direction can be seen in Figures 4.1a to 4.1d. In regions where there is a sudden increase in cross-sectional area, the formation of larger and more coherent vortices can be seen at the inner curvature of the aortic arch due to sudden expansion in area (4.1e to 4.1f). From 0.14 seconds, Figure 4.1g, deceleration makes the flow unstable leading to detachment of vortices from the wall and transportation of the vortices into the middle of the domain. Regions in the domain that see sudden expansion also see the generation of vortices as the flow decelerates.

4.1.2 Transformation of vortices into wall shear stress

Figure 4.2 shows the formation of vortices at the aortic arch and their interaction with the wall. As discussed in previous sections, both wall shear stress as well as vorticity at a particular location are directly proportional to the velocity gradients at the location. As seen in Figure 4.2d, the local spots with high shear stress are spots

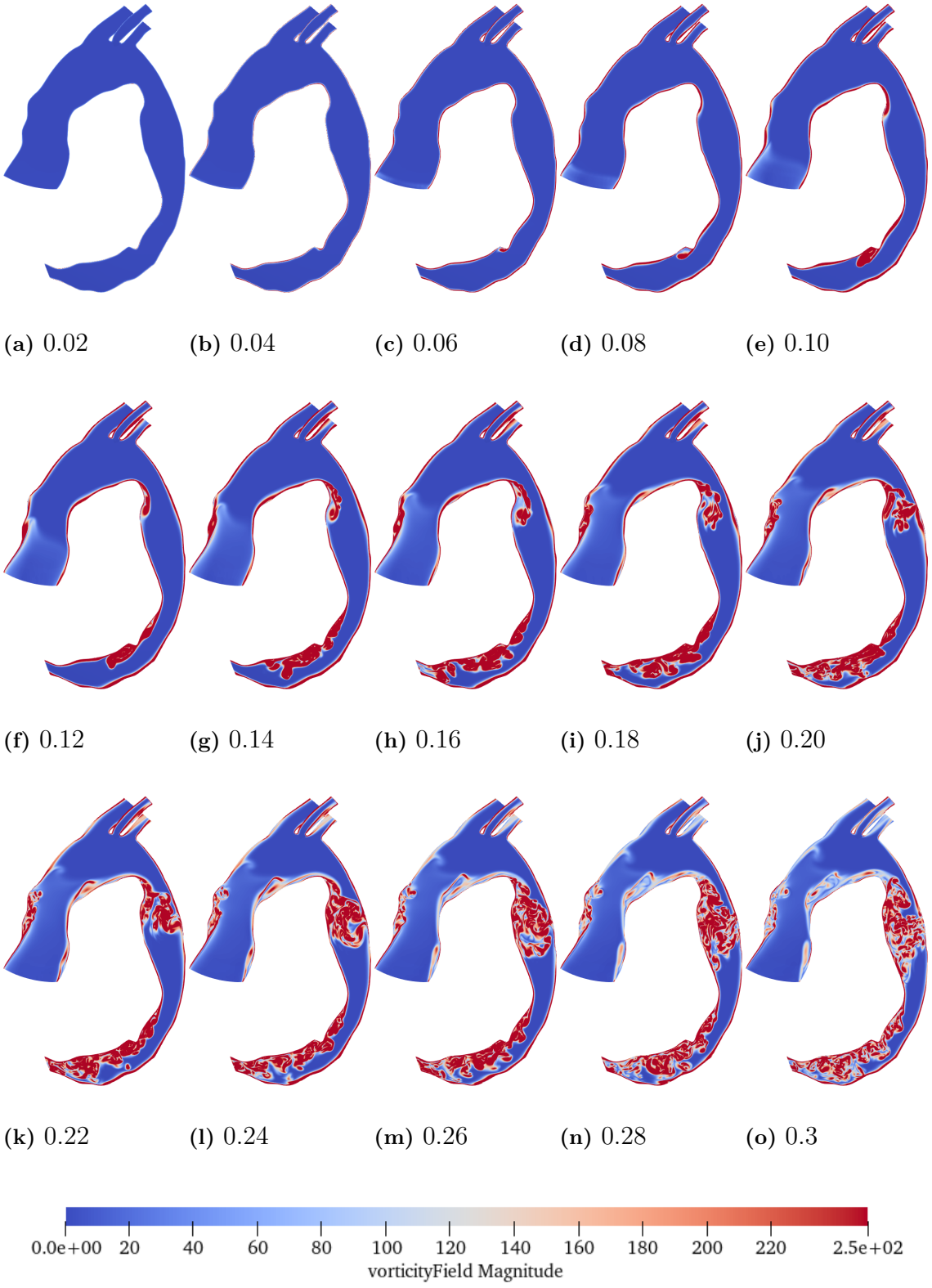

(a) 0.02 **(b)** 0.04 **(c)** 0.06 **(d)** 0.08 **(e)** 0.10

(f) 0.12 **(g)** 0.14 **(h)** 0.16 **(i)** 0.18 **(j)** 0.20

(k) 0.22 **(l)** 0.24 **(m)** 0.26 **(n)** 0.28 **(o)** 0.3

Figure 4.1: Contours of vorticity(1/s) depicted from 0.02s to 0.3s of the cardiac cycle with intervals of 0.02 seconds.Contours plotted on **sectional-view-1** as defined in Section 3.9.

where the vortices are incident on the walls. The stress on the walls are a direct relation to the strength of incident vortices on them. The formation of vortices depend heavily on the geometry of the aorta. Regions with high directional change and high changes in cross-section see higher generation of vortices and subsequently higher magnitude of wall shear stress.

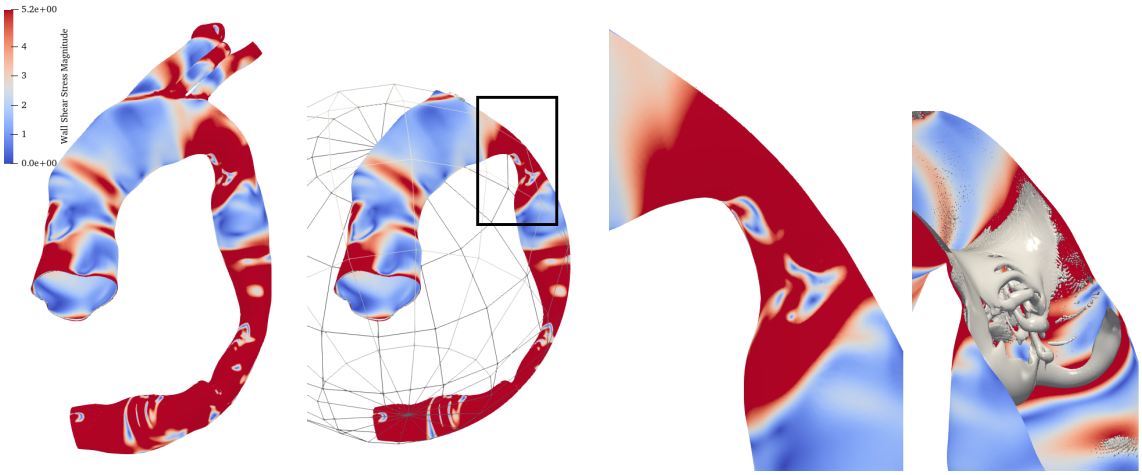

(a) **(b)** **(c)** **(d)**

Figure 4.2: Interaction of vortices on the arterial wall (time stamp: 0.14s), (a) Wall-shear-stress(Pa) scaled to accentuate non negligible stress,(b) definition of spherical clip ,(c) magnified region of the initial region of the descending aorta ,(d) the view in image (c) is rotated and Q-criterion (gray vortical structures) is defined to show the interaction of the vortices with the walls.

4.2 Newtonian model vs non-Newtonian model

Figure 4.3 shows the co-relation between vorticity, shear rate and viscosity at 0.14 seconds of the cardiac cycle. Since vorticity and shear rate are directly proportional to each other, regions where vortices are created (sudden expansion regions and boundary layers) are regions with high shear rates. Since a shear thinning model is employed in this study, viscosity of blood is reduced at high shear rates. This is seen in Figure 4.3c. The effect of the reduction in viscosity can further be visualized as depicted in Figure 4.4, where the reduction in viscosity has made the vortices less coherent, as apposed to a more viscous Newtonian fluid as seen in Figure 4.4b.

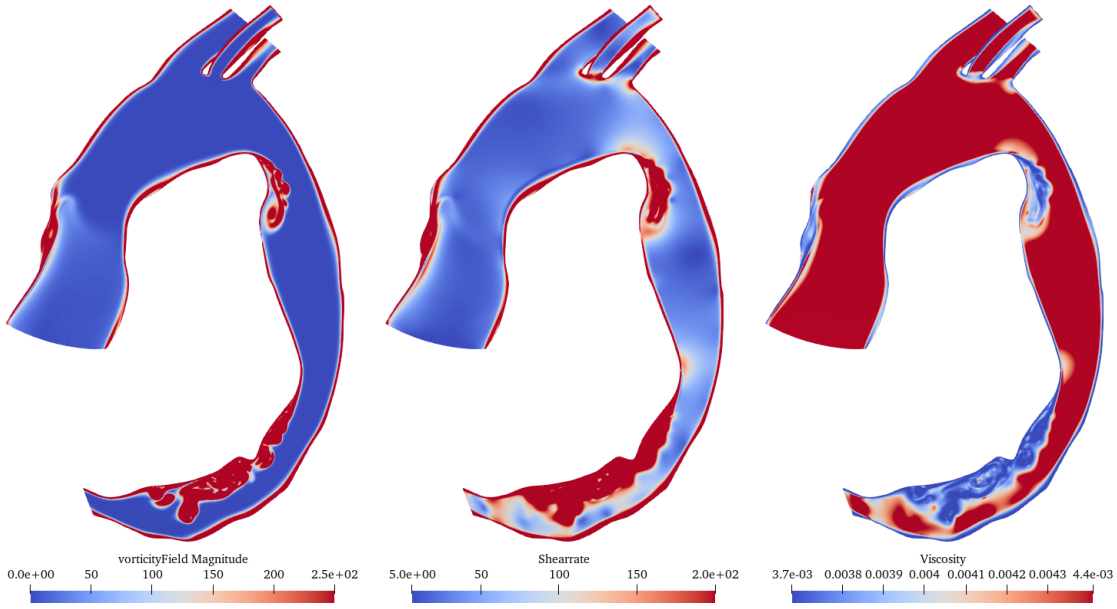

(a) **(b)** **(c)**

Figure 4.3: Non-Newtonian flow features on **sectional-view-1** as defined in Figure 3.9 (time stamp: 0.14s) ,(a) vorticity(1/s) ,(b) shear-rate(1/s) ,(c) viscosity(Pa-s).

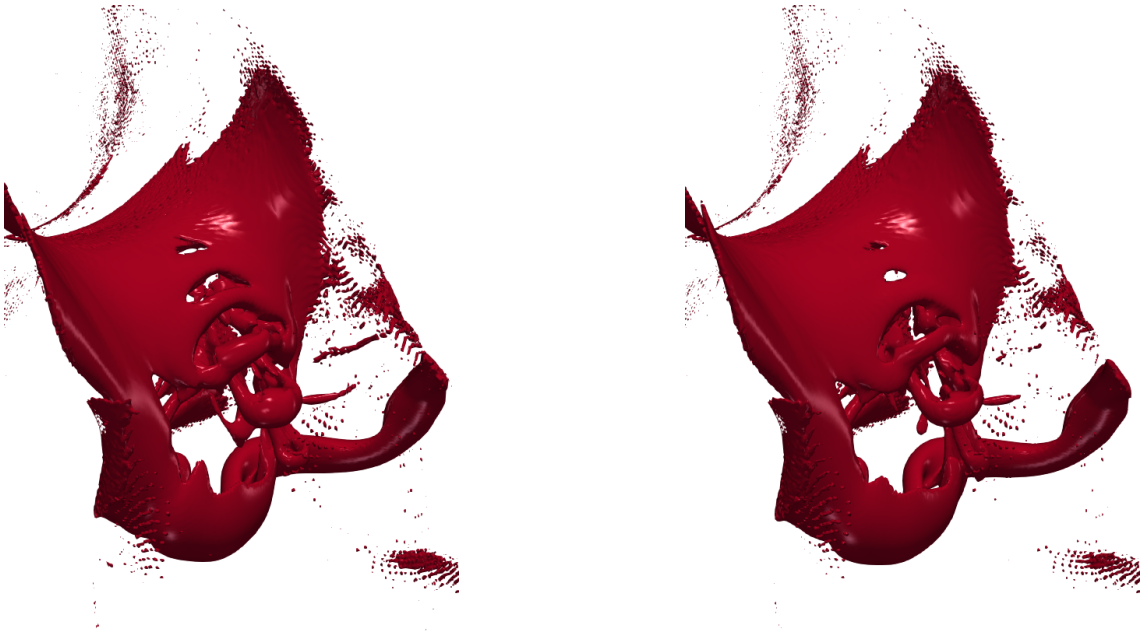

(a) **(b)**

Figure 4.4: Q-criterion at the distal region of the aortic arch as defined in figure 3.9 (time stamp: 0.14s), (a) non-Newtonian model,(b) Newtonian model.

Inner data collection line

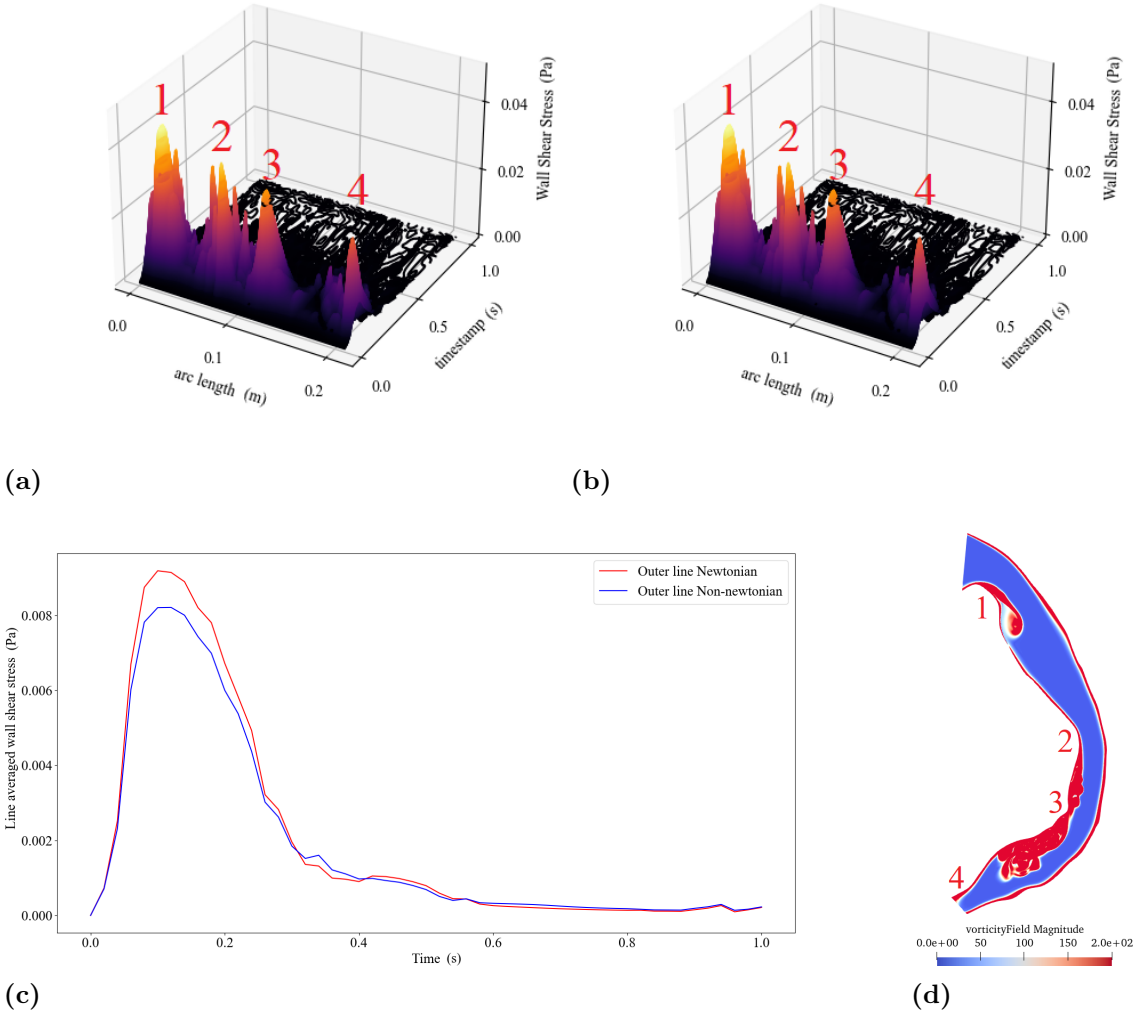

Figure 4.5: Wall shear stress(Pa) comparison on inner data collection line against axis length(m) and time(s), (a) 3D plot of wall shear stress - non-Newtonian , (b) 3D plot of wall shear stress - Newtonian , (c) line averaged wall shear stress comparison, (d) depiction of the data collection curve with points of interest on contour of vorticity(1/s) at time: 0.14s.

Figure 4.5a and 4.5b show the shear stress at the inner curve for the non-Newtonian and the Newtonian assumptions respectively. When seen together with Figure 4.5d, it can be seen that the regions 1,2,3 and 4 have the highest peaks and are also at the locations of increase in downstream area cross-section. From Figure 4.5c, it is seen that the line averaged wall shear stress for the Newtonian case is higher than that of the non-Newtonian case. On time averaging the same curve it is noted that the Newtonian case expressed wall shear stress 7.41% more than the non-Newtonian case. As wall shear stress is a function of viscosity and velocity gradients, a reduction is viscosity at a local region will reduce the wall shear stress at the region.

Outer data collection line

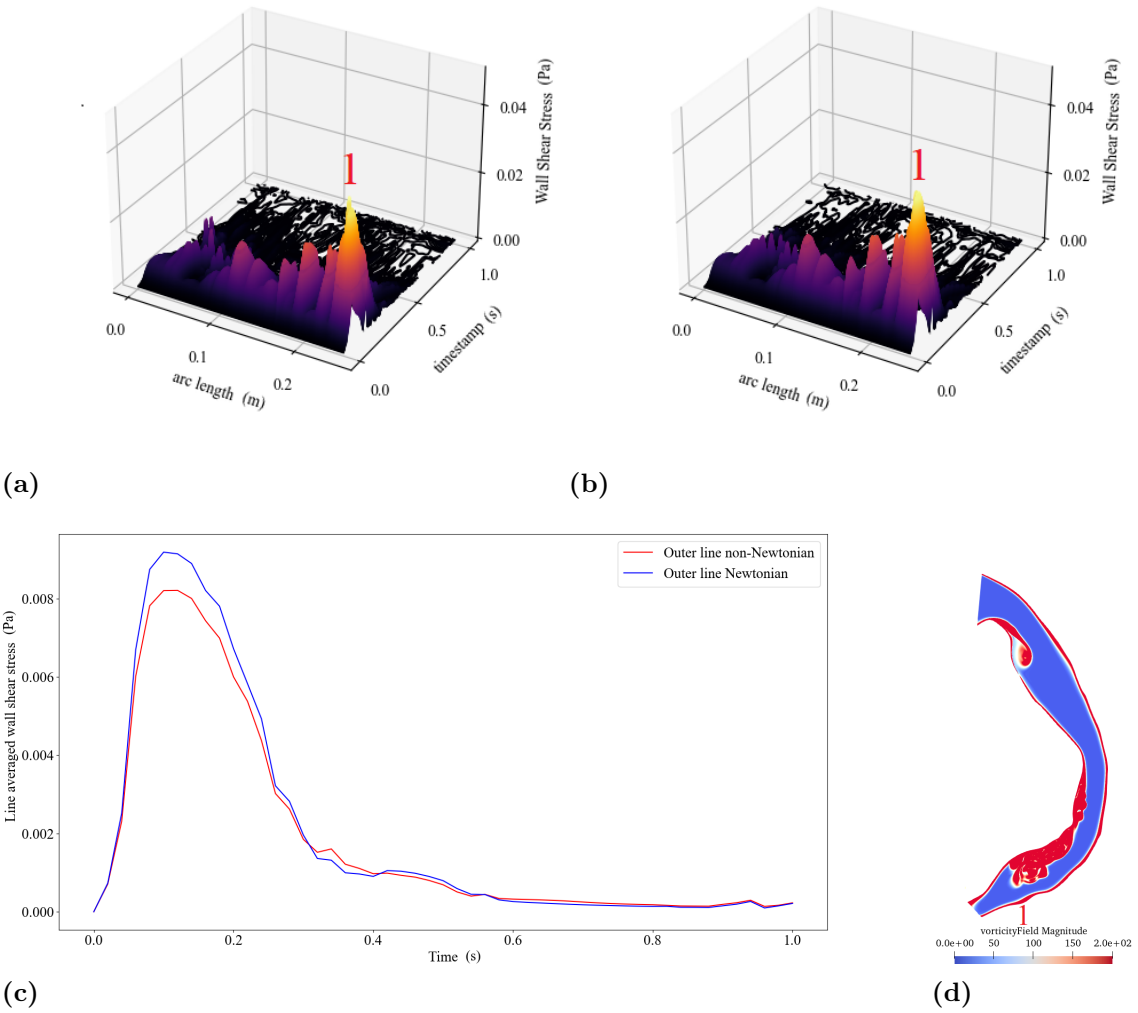

Figure 4.6: Wall shear stress(Pa) comparison on outer data collection line against axis length(m) and time(s), (a) 3D plot of wall shear stress - non-Newtonian, (b) 3D plot of wall shear stress - Newtonian, (c) line averaged wall shear stress comparison, (d) depiction of the data collection curve with points of interest on contour of vorticity(1/s) at time: 0.14s.

Figure 4.6a and 4.6b show the shear stress at the outer curve for the non-Newtonian and the Newtonian assumptions respectively. When seen together with Figure 4.5d, it can be seen that there is only one peak at the distal end of the thoracic aorta (due to an axial twist in the geometry), this can be attributed to the overall smoothness of the outer wall in comparison to the inner wall. From Figure 4.5c, it is seen that the line averaged wall shear stress for the Newtonian case is higher than that of the non-Newtonian case. On time averaging the same curve it is noted that the Newtonian case expressed wall shear stress 6.94% more than the non-Newtonian case.

Anterior data collection line

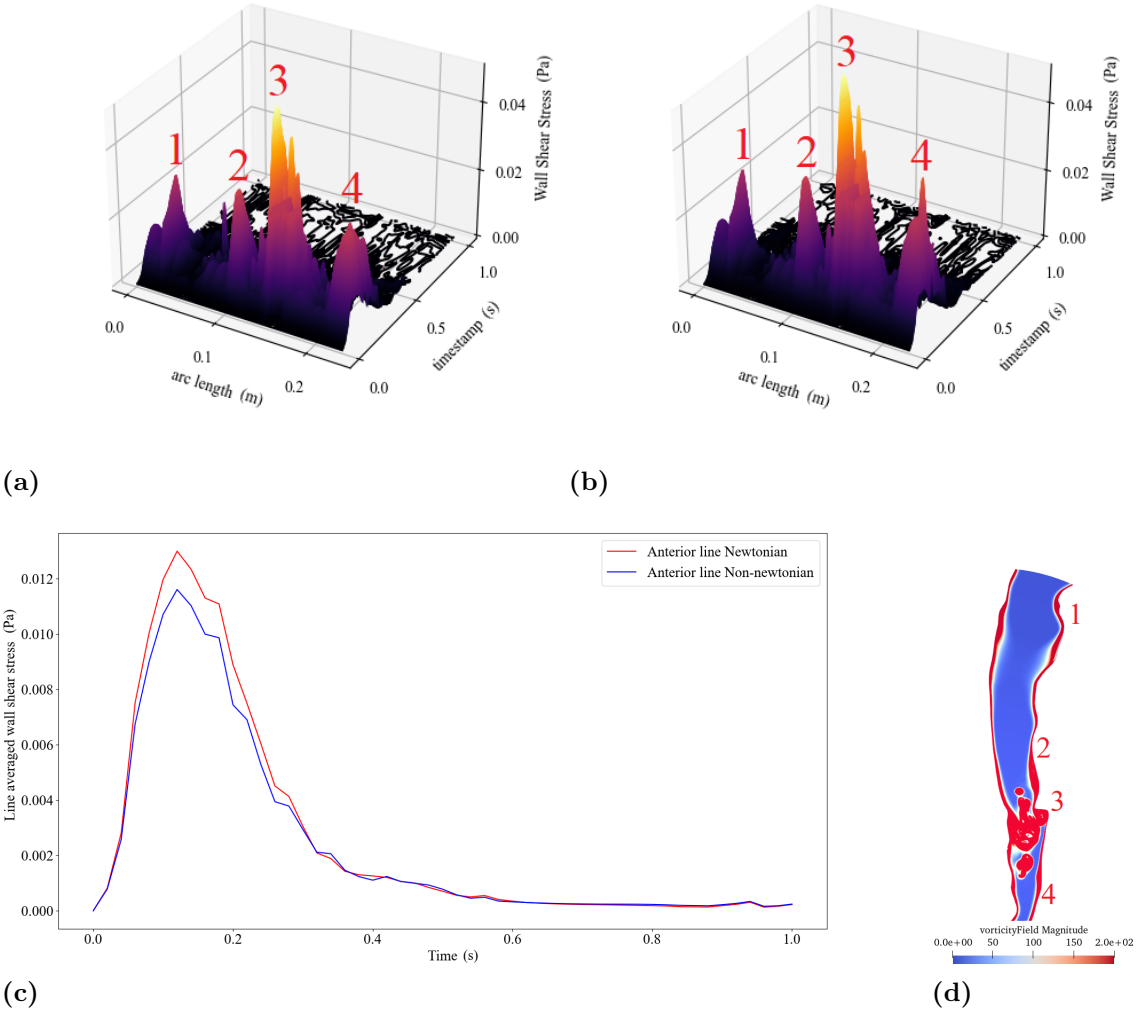

Figure 4.7: Wall shear stress(Pa) comparison on anterior data collection line against axis length(m) and time(s), (a) 3D plot of wall shear stress - non-Newtonian, (b) 3D plot of wall shear stress - Newtonian, (c) line averaged wall shear stress comparison, (d) depiction of the data collection curve with points of interest on contour of vorticity(1/s) at time: 0.14s.

Figure 4.7a and 4.7b show the shear stress at the anterior curve for the non-Newtonian and the Newtonian assumptions respectively. When seen together with Figure 4.7d, it can be seen that the regions 1,2,3 and 4 have the highest peaks, the highest of them being at the the biggest area expansion (point 3). From Figure 4.7c, it is seen that the line averaged wall shear stress for the Newtonian case is higher than that of the non-Newtonian case. On time averaging the same curve it is noted that the Newtonian case expressed wall shear stress 8.7% more than the non-Newtonian case. As wall shear stress is a function of viscosity and velocity gradients, a reduction is viscosity will reduce the wall shear stress.

Posterior data collection line

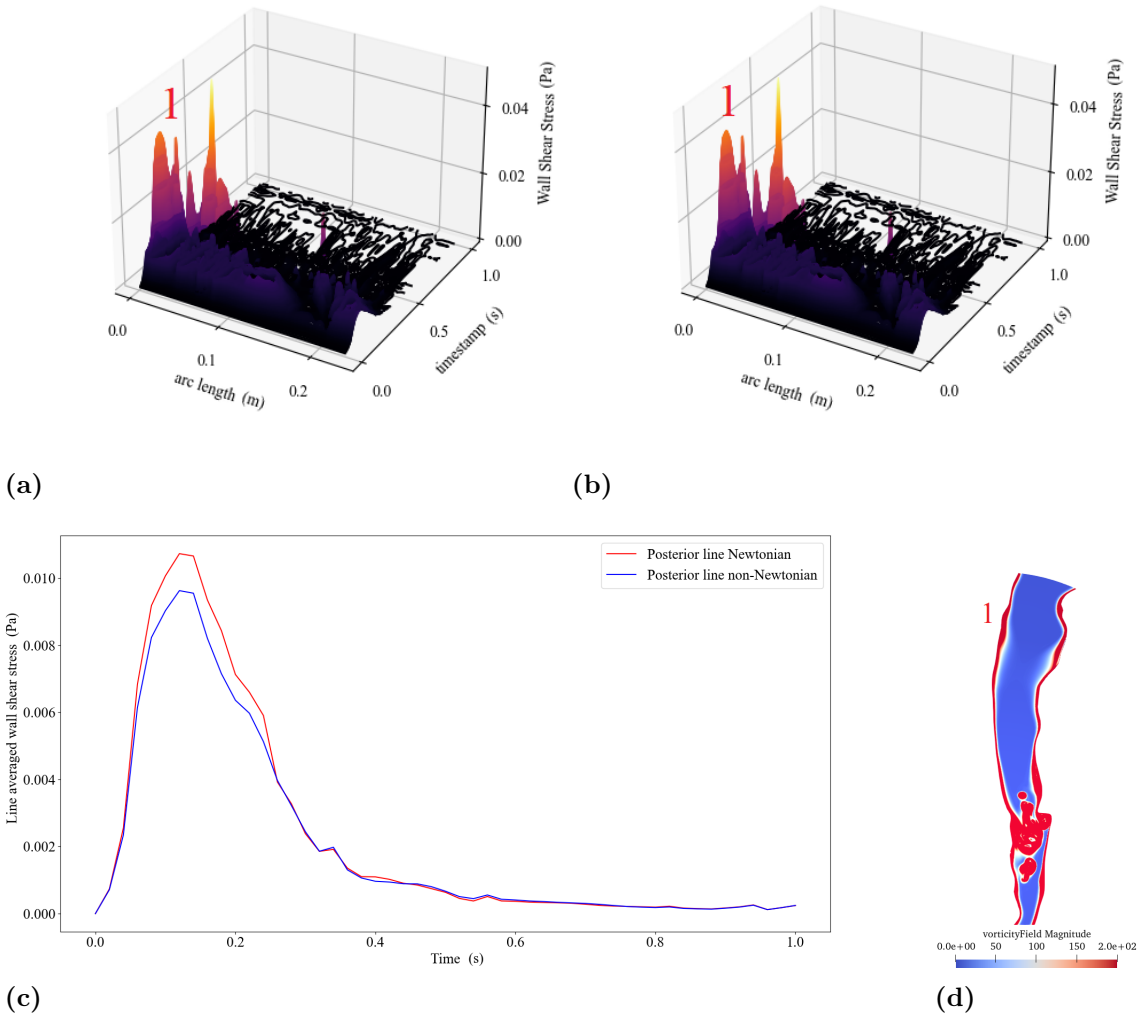

Figure 4.8: Wall shear stress(Pa) comparison on posterior data collection line against axis length(m) and time(s), (a) 3D plot of wall shear stress - non-Newtonian , (b) 3D plot of wall shear stress - Newtonian , (c) line averaged wall shear stress comparison, (d) depiction of the data collection curve with points of interest on contour of vorticity(1/s) at time: 0.14s.

Figure 4.8a and 4.8b show the shear stress at the posterior curve for the non-Newtonian and the Newtonian assumptions respectively. When seen together with Figure 4.8d, it can be seen that there is only one peak at the proximal end of the thoracic aorta (due to its proximity to the aortic arch), the reduction in number of peaks can be attributed to the overall smoothness of the outer wall in comparison to the inner wall. From Figure 4.8c, it is seen that the line averaged wall shear stress for the Newtonian case is higher than that of the non-Newtonian case. On time averaging the same curve it is noted that the Newtonian case expressed wall shear stress 8.17% more than the non-Newtonian case.

4.3 Luminal aorta vs abluminal aorta

Anterior data collection line

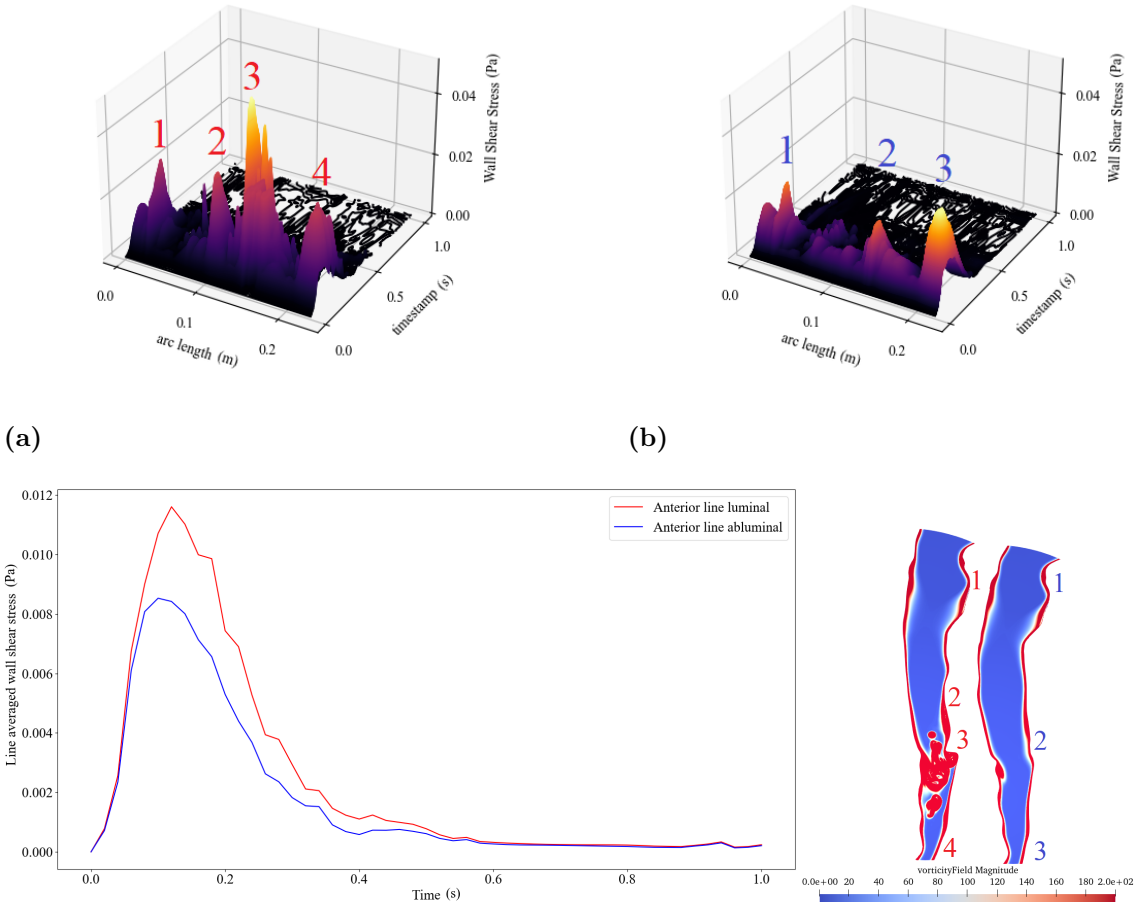

Figure 4.9: Wall shear stress(Pa) comparison on anterior data collection line against axis length(m) and time(s), (a) 3D plot of wall shear stress - luminal - non-Newtonian , (b) 3D plot of wall shear stress - abluminal - non-Newtonian , (c) line averaged wall shear stress comparison, (d) depiction of the data collection curve with points of interest on contour of vorticity(1/s) at time: 0.14s.

Figure 4.9a and 4.9b show the shear stress at the anterior curve for the luminal and abluminal case. When seen together with Figure 4.9d, it can be seen that the regions 1,2,3 and 4 have the highest peaks. The smoothness of the abluminal aorta has resulted in lesser vortices being generated. From Figure 4.9c, it is seen that the line averaged wall shear stress for the luminal case is higher than that of the abluminal case. On time averaging the same curve it is noted that the luminal case expressed wall shear stress 25.9% more than the abluminal case.

Posterior data collection line

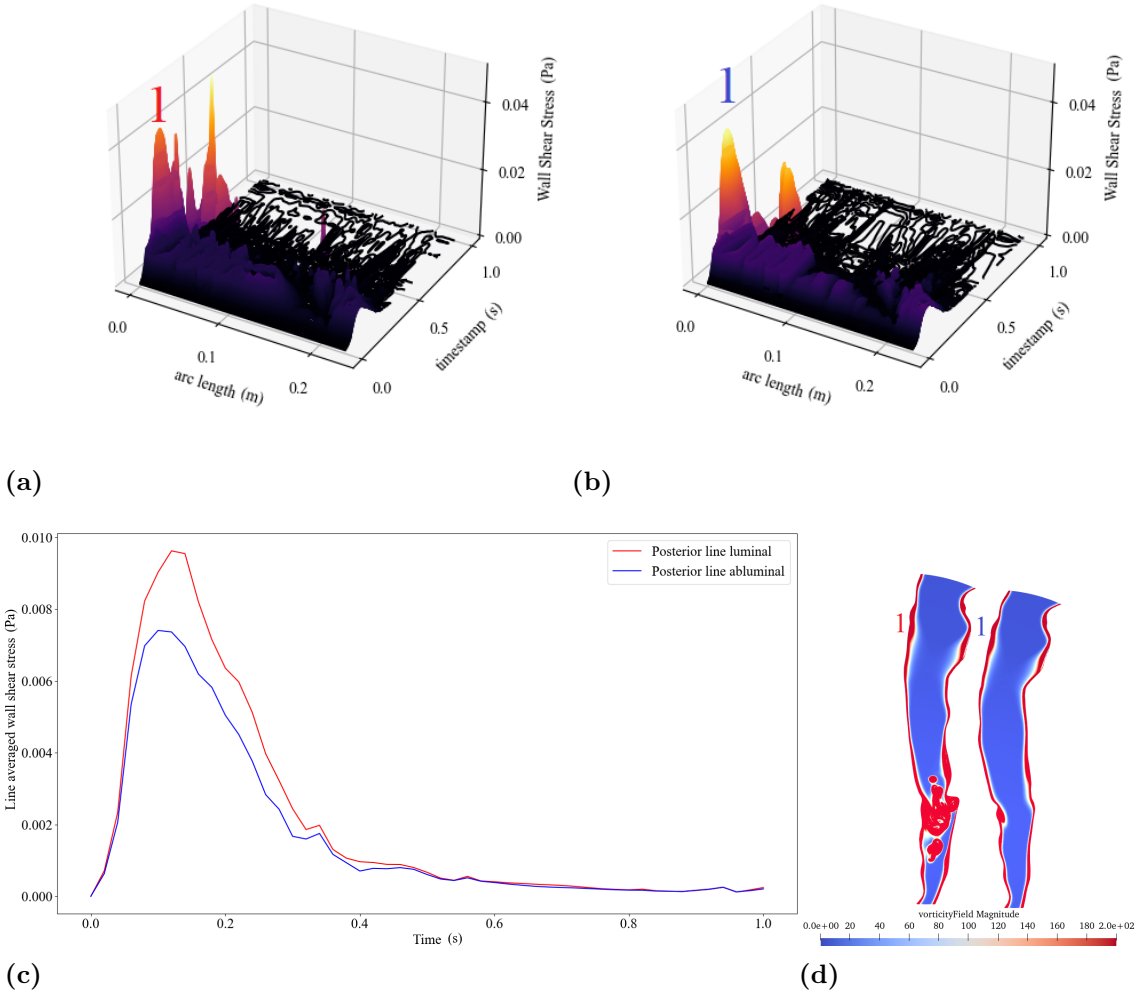

Figure 4.10: Wall shear stress(Pa) comparison on posterior data collection line against axis length(m) and time(s), (a) 3D plot of wall shear stress - luminal - non-Newtonian, (b) 3D plot of wall shear stress - abluminal - non-Newtonian, (c) line averaged wall shear stress comparison, (d) depiction of the data collection curve with points of interest on contour of vorticity(1/s) at time: 0.14s.

Figure 4.10a and 4.10b show the shear stress at the anterior curve for the luminal and abluminal case. When seen together with Figure 4.10d, it can be seen that there is only one peak at the proximal end of the thoracic aorta (due to its proximity to the aortic arch). The difference in the number of peaks with that of the anterior line is due to the smoothness of the posterior line. From Figure 4.10c, it is seen that the line averaged wall shear stress for the luminal case is higher than that of the abluminal case. On time averaging the same curve it is noted that the luminal case expressed wall shear stress 19.8% more than the abluminal case.

Inner data collection line

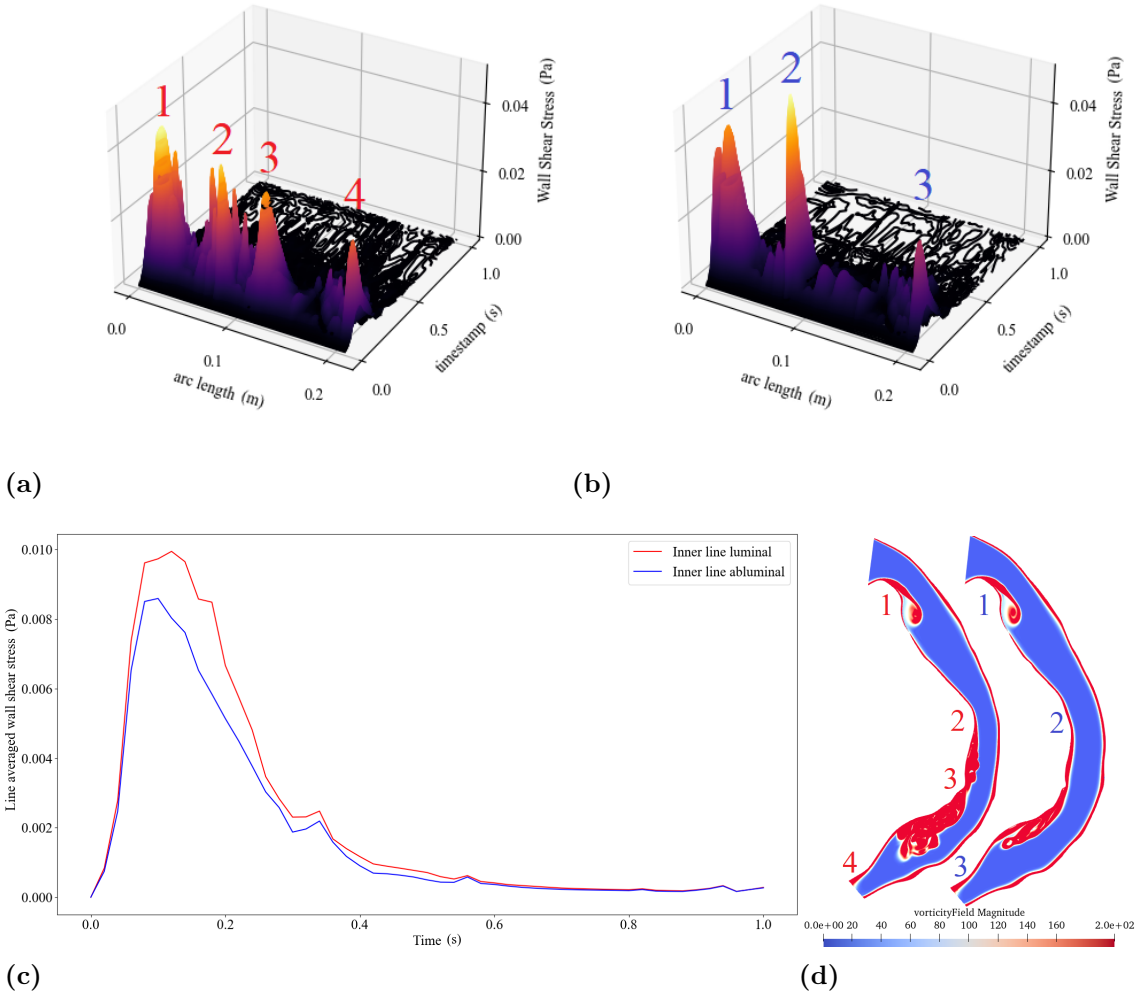

Figure 4.11: Wall shear stress(Pa) comparison on inner data collection line against axis length(m) and time(s), (a) 3D plot of wall shear stress - luminal - non-Newtonian , (b) 3D plot of wall shear stress - abluminal - non-Newtonian ,(c) line averaged wall shear stress comparison, (d) depiction of the data collection curve with points of interest on contour of vorticity(1/s) at time: 0.14s.

Figure 4.11a and 4.11b show the shear stress at the inner curve for the luminal and the abluminal case. When seen together with Figure 4.11d, it can be seen that there are multiple peaks of high shear stress in the luminal case. From Figure 4.11c, it is seen that the line averaged wall shear stress for the luminal case is higher than that of the abluminal case. On time averaging the same curve it is noted that the luminal case expressed wall shear stress 17.8% more than the abluminal case.

Outer data collection line

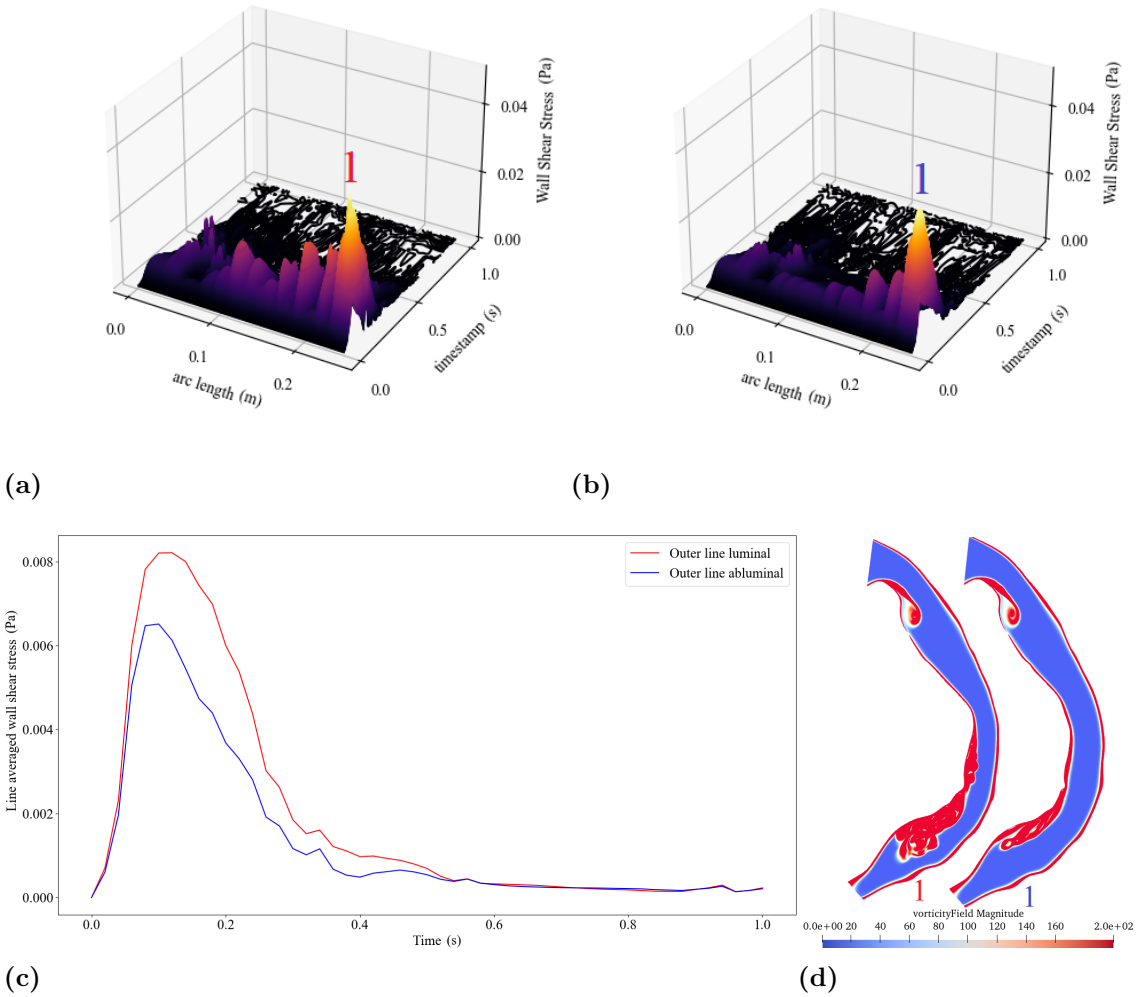

Figure 4.12: Wall shear stress(Pa) comparison on outer data collection line against axis length(m) and time(s), (a) 3D plot of wall shear stress - luminal - non-Newtonian , (b) 3D plot of wall shear stress - abluminal - non-Newtonian ,(c) line averaged wall shear stress comparison, (d) depiction of the data collection curve with points of interest on contour of vorticity(1/s) at time: 0.14s.

Figure 4.12a and 4.12b show the shear stress at the outer curve for the luminal and abluminal case. When seen together with Figure 4.12d, it can be seen that there are multiple peaks of high shear stress near the distal ends of the aorta (due to axial twisting of the geometry). From Figure 4.12c, it is seen that the line averaged wall shear stress for the luminal case is higher than that of the abluminal case. On time averaging the same curve it is noted that the luminal case expressed wall shear stress 17.8% more than the abluminal case.

4.4 Discussions

Wall shear stress	Newtonian > non-Newtonian	Luminal > abluminal
Anterior curve	8.7%	17.8%
Posterior curve	8.17%	25.9%
Inner curve	7.41%	19.8%
Outer curve	6.94%	17.8%
Average	7.80%	20.32%

Table 4.1: Comparison of wall shear stress values along the four data collections lines under the two studies. Column 1 depicts the percentage difference between the Newtonian and the non-Newtonian viscosity approximation. Column 2 depicts the percentage difference between the luminal and the abluminal geometries.

The velocity profiles from the validation study as presented in Section 3.4 show good coherence with experimental results conducted on a blood analogous fluid (xanthangum in potassium thiocyanata and water) synthesized to mimic the shear thinning behaviour of blood flow at shear rates encountered in human arteries and arterioles. The validation study also compares velocity profiles between CFD data with a constant viscosity model and experimental data conducted on a Newtonian fluid (potassium thiocyanata without xanthangum) synthesized to have a viscosity equal to that of blood seen in extremely high shear rates where blood behaves like a Newtonian fluid. The shear thinning nature of blood, which reduces viscosity under increasing shear rates and increases viscosity under reducing shear rates, can be clearly seen in the smoother velocity gradients in the non-Newtonian velocity profiles. A significant difference between the velocity profiles and viscosities of blood as a Newtonian fluid and as a non-Newtonian fluid mean that any quantity that is derived from velocity and viscosity such as vorticity and wall shear stress will also show significant differences based on how its rheology is modelled.

Column 1 in Figure 4.1 shows the percentage difference in the magnitude of wall shear stress between the Newtonian and the non-Newtonian assumption. The non-Newtonian assumption has wall shear stresses lesser than the Newtonian assumption on an average of 7.80%. The reason for the over-expression of wall shear stress in the Newtonian assumption has to do with the absence of shear thinning. As wall shear stress is a function of velocity gradients and viscosity, shear thinning reduces the shear stress induced on the walls. The anterior data collection lines has the highest difference in wall shear stresses (8.7%) because it runs through the region of malapposition of the two endografts. The high shear rates that are observed at the region of the malapposition causes the viscosity to reduce in the non-Newtonian model. The absence of the reduction in viscosity in the Newtonian model forces the wall shear stress to have higher values.

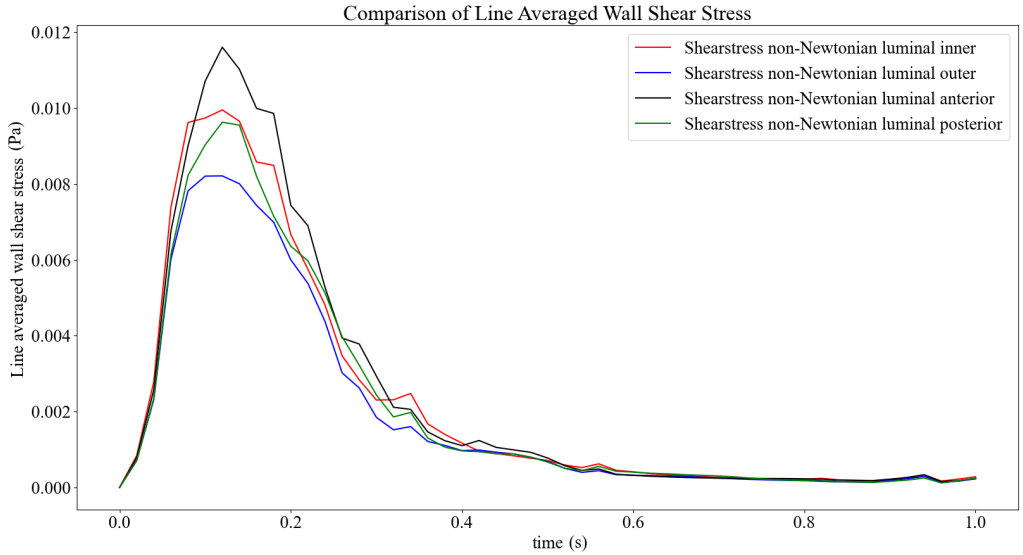

Figure 4.13: Line averaged wall shear stress(Pa) plotted against time(s) for different data collection curves.

The anterior data collection line as observed in several figures in the previous sections has the most rugged surface with several regions of sudden expansion, including the region of malapposition of the two endografts. The outer data collection curve however has the smoothest surface amongst other data collection curves. Along with viscosity, wall shear stress is a function of velocity gradients. Velocity gradients are high in rotational flow with high vorticity. High rotational flows are seen in regions of sudden expansion and regions where the flow is forced to change it's orientation (twisting and bending of the wall). Therefore, it makes sense that the anterior data collection curve must have the highest wall shear stress as compared to the other curves. Figure 4.13 shows that the the wall shear stress on the anterior data collection curve is the highest followed by the inner, posterior and outer data collection curves.

The abluminal aortic geometry eliminates the malapposition of the two endografts and considers a smooth transition between its surfaces. Based on the arguments discussed in the previous paragraph, the higher smoothness of the abluminal aorta must result in lower wall shear stresses on its walls. Column 2 in Table 4.1 shows the percentage difference in the magnitude of wall shear stress between the luminal and the abluminal geometries. The abluminal assumption has wall shear stresses lesser than the luminal assumption on an average of 20.32%. Looking at Table 4.1, one can assume that the effect of change in the surface features is more than the choice of rheological model, however, it might be the case for this particular patient.

The different arguments discussed above shed light on the effect and importance of geometrical features of the aortic wall and rheological treatment of blood in the prediction of wall shear stress. As reported in Section 1.1, wall shear stress can plays a significant role in the pathophysiology of aortic conditions like dissections and aneurysms as well as post-TEVAR complications such as endograft migration and endoleaks. Therefore, the two main deductions can be as follows, 1. accurate

predictions of wall shear stress require accurate treatment of the viscosity of blood, 2. A lumen surface post-TEVAR which is smoother will introduce lesser vortices into the flow and subsequently will have lower shear stress on its walls, therefore, it will be less likely to have future complications which are induced by high wall shear stress.

5
Conclusion

An attempt to understand the rheology of blood and its flow in dissected aortas that have undergone TEVAR was made using computational fluid dynamics.

Based on the results presented in the validation study of this thesis, it can be said that the methodology followed in this thesis to predict velocity and viscosity as well as its derived quantities such as vorticity and wall shear stress is viable.

The formation of vortices as well as the shear stress on the walls significantly depend on the path of blood as well as the evenness of the surface. Regions of sudden expansion and contraction as well as regions of high directional change introduce the most vortices into the domain. Therefore, irregular area changes in the lumen that are a result of natural diseases, malapposition of implants, malapposition of overlapping implants and natural change due to old age will cause significantly higher shear stress on the walls.

The CFD methodology used in this thesis can be implemented to predict the possible location of wall shear stress induced conditions in the aorta such as aneurysms or dissections. Simulations of blood flow in an aorta after implants are surgically placed can help predict the location of wall shear stress induced complications such as graft migration and endoleaks. However, it must be noted that the findings of this thesis is inside the scope of predicting the accurate value of shear stress at different locations and not the accurate pathophysiology of diseases.

Wall shear stress is directly proportional to the viscosity of blood incident on the wall. Therefore, it is important that the local viscosity of blood is accurately predicted. The Carreau-Yasuda model treats blood as non-Newtonian fluid in a window of wall shear stresses and treats blood as a Newtonian fluid outside the above mentioned window. Therefore, the model can be used to accurately predict the local viscosity of shear induced blood.

5.1 Future work

To gain more validation in the methods used, it would be very valuable to compare CFD results with actual clinical data for the same geometry, as in the current study validation with experimental results are done for the carotid bifurcation, rather that the aorta.

The thesis discusses extensively on the role of geometrical features in the prediction of wall shear stress, therefore, it will be very beneficial to treat the aortic walls as a non-rigid entity that can deform and interact with the blood flow.

As opposed to modelling the viscous effects in blood, getting out of continuum and treating blood as a multi-phase fluid with the ability of its particles to interact chemically and mechanically with each other and their surroundings would provide a deeper insight into the complex rheology of blood.

Bibliography

[1] World health organization, cardiovascular diseases (cvds), https://www.who.int/news-room/fact-sheets/detail/cardiovascular-diseases-(cvds).

[2] Philip I Aaronson, Jeremy PT Ward, and Michelle J Connolly. *The cardiovascular system at a glance*. John Wiley & Sons, 2020.

[3] Wan Naimah Wan Ab Naim, Poo Balan Ganesan, Zhonghua Sun, Yih Miin Liew, Yi Qian, Chang-Joon Lee, Shirley Jansen, Shahrul Amry Hashim, and Einly Lim. Prediction of thrombus formation using vortical structures presentation in stanford type b aortic dissection: a preliminary study using cfd approach. *Applied Mathematical Modelling*, 40(4):3115–3127, 2016.

[4] I Akin, S Kische, TC Rehders, H Schneider, H Ince, and CA Nienaber. Tevar. *Herz*, 36(6):539, 2011.

[5] Jordi Alastruey, Nan Xiao, Henry Fok, Tobias Schaeffter, and C Alberto Figueroa. On the impact of modelling assumptions in multi-scale, subject-specific models of aortic haemodynamics. *Journal of The Royal Society Interface*, 13(119):20160073, 2016.

[6] F Auricchio, M Conti, A Lefieux, S Morganti, A Reali, F Sardanelli, F Secchi, S Trimarchi, and A Veneziani. Patient-specific analysis of post-operative aortic hemodynamics: a focus on thoracic endovascular repair (tevar). *Computational Mechanics*, 54(4):943–953, 2014.

[7] Jacopo Biasetti, Fazle Hussain, and T Christian Gasser. Blood flow and coherent vortices in the normal and aneurysmatic aortas: a fluid dynamical approach to intra-luminal thrombus formation. *Journal of The Royal Society Interface*, 8(63):1449–1461, 2011.

[8] Robert Byron Bird, Robert Calvin Armstrong, and Ole Hassager. Dynamics of polymeric liquids. vol. 1: Fluid mechanics. 1987.

[9] JOHAN BONDESSON. Geometric modeling of thoracic aortic surface morphology.

[10] Johan Bondesson, Ga-Young Suh, Neil Marks, Michael D Dake, Jason T Lee, and Christopher P Cheng. Influence of thoracic endovascular aortic repair

on true lumen helical morphology for stanford type b dissections. *Journal of Vascular Surgery*, 2021.

[11] KA Brookshier and JM Tarbell. Evaluation of a transparent blood analog fluid: aqueous xanthan gum/glycerin. *Biorheology*, 30(2):107–116, 1993.

[12] https://Blausen.com Bruce Blaus, CC BY-SA 3.0.

[13] https://commons.wikimedia.org/w/index.php?curid=18764854 By DanielChangMD revised original work of DestinyQx; Redrawn as SVG by xavax Wikimedia Commons, CC BY-SA 2.5. *Wiggers Diagram.*

[14] https://commons.wikimedia.org/w/index.php?curid=25142709 By g-sec Own work, CC BY-SA 3.0. *Rheology of time independent fluids.*

[15] https://wellcomecollection.org/works/h5eshqtg By Jonathan Armstrong, CC BY-NC 4.0. *Red blood cells forming rouleaux.*

[16] Marcus Vinicius Paes Carvalho, Raquel Jahara Lobosco, and Guilherme Barbosa Lopes Júnior. Rheological analysis of blood flow in the bifurcation of carotid artery with openfoam. In *Brazilian Technology Symposium*, pages 223–230. Springer, 2018.

[17] E Choke, G Cockerill, WRW Wilson, S Sayed, J Dawson, I Loftus, and MM Thompson. A review of biological factors implicated in abdominal aortic aneurysm rupture. *European Journal of Vascular and Endovascular Surgery*, 30(3):227–244, 2005.

[18] Dania Daye and T Gregory Walker. Complications of endovascular aneurysm repair of the thoracic and abdominal aorta: evaluation and management. *Cardiovascular diagnosis and therapy*, 8(Suppl 1):S138, 2018.

[19] Kim A Eagle and Roman W DeSanctis. Aortic dissection. *Current problems in cardiology*, 14(5):225–278, 1989.

[20] Mustafa Etli, Gokhan Canbolat, Oguz Karahan, and Murat Koru. Numerical investigation of patient-specific thoracic aortic aneurysms and comparison with normal subject via computational fluid dynamics (cfd). *Medical & Biological Engineering & Computing*, 59(1):71–84, 2021.

[21] Aortic Dissection By Mark A. Farber, By, Mark A. Farber, Federico E Parodi, and Last full review/revision Nov 2020| Content last modified Nov 2020. Aortic dissection - cardiovascular disorders.

[22] Joanna Gawinecka, Felix Schönrath, and Arnold von Eckardstein. Acute aortic dissection: pathogenesis, risk factors and diagnosis. *Swiss medical weekly*, 147:w14489, 2017.

[23] Glaucylara Reis Geovanini and Peter Libby. Atherosclerosis and inflammation: overview and updates. *Clinical Science*, 132(12):1243–1252, 2018.

[24] DP Giddens, CK Zarins, and S Glagov. The role of fluid mechanics in the localization and detection of atherosclerosis. 1993.

[25] Frank JH Gijsen, Frans N van de Vosse, and JD Janssen. The influence of the non-newtonian properties of blood on the flow in large arteries: steady flow in a carotid bifurcation model. *Journal of biomechanics*, 32(6):601–608, 1999.

[26] Leonid Goubergrits, Eugenie Riesenkampff, Pavlo Yevtushenko, Jens Schaller, Ulrich Kertzscher, Anja Hennemuth, Felix Berger, Stephan Schubert, and Titus Kuehne. Mri-based computational fluid dynamics for diagnosis and treatment prediction: Clinical validation study in patients with coarctation of aorta. *Journal of Magnetic Resonance Imaging*, 41(4):909–916, 2015.

[27] Peter G Hagan, Christoph A Nienaber, Eric M Isselbacher, David Bruckman, Dean J Karavite, Pamela L Russman, Arturo Evangelista, Rossella Fattori, Toru Suzuki, Jae K Oh, et al. The international registry of acute aortic dissection (irad): new insights into an old disease. *Jama*, 283(7):897–903, 2000.

[28] Yu Hohri, Satoshi Numata, Keiichi Itatani, Keiichi Kanda, Sachiko Yamazaki, Tomoya Inoue, and Hitoshi Yaku. Prediction for future occurrence of type a aortic dissection using computational fluid dynamics. *European Journal of Cardio-Thoracic Surgery*, 2021.

[29] HA Krebs. Chemical composition of blood plasma and serum. *Annual review of biochemistry*, 19(1):409–430, 1950.

[30] Z Kulcsár, E Houdart, A Bonafé, G Parker, J Millar, AJP Goddard, S Renowden, G Gal, B Turowski, K Mitchell, et al. Intra-aneurysmal thrombosis as a possible cause of delayed aneurysm rupture after flow-diversion treatment. *American Journal of Neuroradiology*, 32(1):20–25, 2011.

[31] Armin Leuprecht and Karl Perktold. Computer simulation of non-newtonian effects on blood flow in large arteries. *Computer Methods in Biomechanics and Biomedical Engineering*, 4(2):149–163, 2001.

[32] Jichun Li, Todd Arbogast, and Yunqing Huang. Mixed methods using standard conforming finite elements. *Computer methods in applied mechanics and engineering*, 198(5-8):680–692, 2009.

[33] Adel M Malek, Seth L Alper, and Seigo Izumo. Hemodynamic shear stress and its role in atherosclerosis. *Jama*, 282(21):2035–2042, 1999.

[34] Marco Midulla, Ramiro Moreno, Adil Baali, Ming Chau, Anne Negre-Salvayre, Franck Nicoud, Jean-Pierre Pruvo, Stephan Haulon, and Hervé Rousseau. Haemodynamic imaging of thoracic stent-grafts by computational fluid dynamics (cfd): presentation of a patient-specific method combining magnetic resonance imaging and numerical simulations. *European radiology*, 22(10):2094–2102, 2012.

[35] Marco Midulla, Ramiro Moreno, Anne Negre-Salvayre, Jean-Paul Beregi, Stéphan Haulon, Romaric Loffroy, Michael Dake, and Hervé Rousseau. Impact of thoracic endografting on the hemodynamics of the native aorta: Pre-and postoperative assessments of wall shear stress and vorticity using computational fluid dynamics. *Journal of Endovascular Therapy*, 28(1):63–69, 2021.

[36] A Polanczyk, A Piechota-Polanczyk, Ch Neumayer, and I Huk. Cfd reconstruction of blood hemodynamic based on a self-made algorithm in patients with acute type iiib aortic dissection treated with tevar procedure. In *IUTAM Symposium on Recent Advances in Moving Boundary Problems in Mechanics*, pages 75–84. Springer, 2019.

[37] Andrzej Polanczyk, Aleksandra Piechota-Polanczyk, Christoph Domenig, Josif Nanobachvili, Ihor Huk, and Christoph Neumayer. Computational fluid dynamic accuracy in mimicking changes in blood hemodynamics in patients with acute type iiib aortic dissection treated with tevar. *Applied Sciences*, 8(8):1309, 2018.

[38] Digvijay S Rawat, Mathieu Pourquie, and Christian Poelma. Numerical investigation of turbulence in abdominal aortic aneurysms. *Journal of biomechanical engineering*, 141(6):061001, 2019.

[39] RM Romarowski, E Faggiano, M Conti, A Reali, S Morganti, and F Auricchio. A novel computational framework to predict patient-specific hemodynamics after tevar: integration of structural and fluid-dynamics analysis by image elaboration. *Computers & Fluids*, 179:806–819, 2019.

[40] Raphael Rubin, David S Strayer, Emanuel Rubin, et al. *Rubin's pathology: clinicopathologic foundations of medicine*. Lippincott Williams & Wilkins, 2008.

[41] Joseph F Sabik, Bruce W Lytle, Eugene H Blackstone, Patrick M McCarthy, Floyd D Loop, and Delos M Cosgrove. Long-term effectiveness of operations for ascending aortic dissections. *The Journal of thoracic and cardiovascular surgery*, 119(5):946–964, 2000.

[42] https://smart.servier.com Servier Medical Arts, CC BY-SA 3.0.

[43] Mariana Simão, Jorge Ferreira, António C Tomás, José Fragata, and Helena Ramos. Aorta ascending aneurysm analysis using cfd models towards possible anomalies. *Fluids*, 2(2):31, 2017.

[44] Taha Sochi. Non-newtonian rheology in blood circulation. *arXiv preprint arXiv:1306.2067*, 2013.

[45] Eduardo Soudah, EYK Ng, TH Loong, Maurizio Bordone, Uei Pua, and Sriram Narayanan. Cfd modelling of abdominal aortic aneurysm on hemodynamic loads using a realistic geometry with ct. *Computational and Mathematical Methods in Medicine*, 2013, 2013.

[46] Zhonghua Sun and Thanapong Chaichana. A systematic review of computational fluid dynamics in type b aortic dissection. *International journal of cardiology*, 210:28–31, 2016.

[47] Adam Updegrove, Nathan M Wilson, Jameson Merkow, Hongzhi Lan, Alison L Marsden, and Shawn C Shadden. Simvascular: an open source pipeline for cardiovascular simulation. *Annals of biomedical engineering*, 45(3):525–541, 2017.

[48] Guido HW Van Bogerijen, Ferdinando Auricchio, Michele Conti, Adrien Lefieux, Alessandro Reali, Alessandro Veneziani, Jip L Tolenaar, Frans L Moll, Vincenzo Rampoldi, and Santi Trimarchi. Aortic hemodynamics after thoracic endovascular aortic repair, with particular attention to the bird-beak configuration. *Journal of Endovascular Therapy*, 21(6):791–802, 2014.

[49] Myron W Wheat Jr. Pathogenesis of aortic dissection. *Aortic Dissection.*, pages 55–60, 1983.

DEPARTMENT OF SOME SUBJECT OR TECHNOLOGY
CHALMERS UNIVERSITY OF TECHNOLOGY
Gothenburg, Sweden
www.chalmers.se

CHALMERS
UNIVERSITY OF TECHNOLOGY